In vivo visualization of propagating α-synuclein pathologies in mouse and marmoset models by a bimodal imaging probe, C05-05

AUTHORS/AFFILIATIONS

Maiko Ono[1,3]*, Manami Takahashi[1,3], Aki Shimozawa[2], Masayuki Fujinaga[1], Wakana Mori[1], Yuji Nagai[1], Koki Mimura[1], Takeharu Minamihisamatsu[1], Shoko Uchida[1], Masafumi Shimojo[1], Yuhei Takado[1], Hiroyuki Takuwa[1], Naruhiko Sahara[1], Ming-Rong Zhang[1], Takafumi Minamimoto[1], Masato Hasegawa[2], Makoto Higuchi[1]

[1]National Institute of Radiological Sciences, National Institutes for Quantum and Radiological Science and Technology, Chiba 263-8555, Japan
[2]Department of Dementia and Higher Brain Function, Tokyo Metropolitan Institute of Medical Science, Tokyo 156-8506, Japan
[3]These authors contributed equally
* Correspondence: ono.maiko@qst.go.jp (M.O.)

SUMMARY

Deposition of intracellular α-synuclein fibrils is implicated in neurodegenerative parkinsonian disorders, while high-contrast *in vivo* detection of α-synuclein depositions has been unsuccessful in animal models and humans. Here, we have developed a bimodal imaging probe, C05-05, for visualizing α-synuclein inclusions in the brains of living animals modeling α-synuclein propagation. *In vivo* optical and PET imaging of a mouse model demonstrated sensitive detection of α-synuclein aggregates by C05-05, revealing a dynamic propagation of fibrillogenesis along neural pathways followed by disruptions of these structures. Moreover, longitudinal ^{18}F-C05-05-PET of a marmoset model captured widespread dissemination of fibrillary pathologies accompanied by neurodegeneration detected by dopamine transporter PET. In addition, *in vitro* assays demonstrated the high-affinity binding of ^{18}F-C05-05 to α-synuclein

versus other protein pathologies in human brain tissues. Collectively, we propose a new imaging technology enabling etiological and therapeutic assessments of α-synuclein pathogenesis at nonclinical levels, highlighting the applicability of C05-05 to clinical PET.

KEY WORDS: α-synuclein, *in vivo* neuroimaging, PET, intravital two-photon microscopy, propagation, mouse model, marmoset model, dementia with Lewy bodies, multiple system atrophy

INTRODUCTION

Parkinson's disease (PD) and dementia with Lewy bodies (DLB) are neurodegenerative diseases of high prevalence, and they are pathologically characterized by the appearance of Lewy bodies and Lewy neurites, which are mainly composed of aggregated α-synuclein (Spillantini et al., 1998b; Baba et al., 1998; Goedert, 2001). Abnormal α-synuclein is also a major component of glial cytoplasmic inclusions (GCIs), which are a pathological feature of multiple system atrophy (MSA), a neurodegenerative disease presenting with movement and autonomic disorders (Spillantini et al., 1998a; Wakabayashi et al., 1998a). In these disorders, referred to as α-synucleinopathies, ultrastructures of α-synuclein filaments containing β-pleated sheets (Serpell et al., 2000) may display diversity in disease-specific and individually variable manners as revealed by the latest cryo-electron microscopic analysis (Schweighauser et al., 2020). Previous studies experimentally demonstrated that α-synuclein fibrils acted as templates for the conversion of normal α-synuclein molecules into misfolded species, leading to the prion-like propagation of the α-synuclein fibrillogenesis throughout the brain via neural circuits (Luk et al., 2012a and 2012b; Masuda-Suzukake et al., 2013 and 2014).

Formation of intracellular α-synuclein fibrils is mechanistically linked to neurodegenerative processes, and the spread of α-synuclein inclusions in the brain is supposed to be the neuropathological basis of the disease progression (Braak et al., 2003; Saito et al., 2003; Henderson et al., 2019), supporting the significance of the α-synuclein assembly as a diagnostic and staging biomarker and a therapeutic target. Meanwhile, the diagnosis of PD, DLB, and MSA can only be confirmed by examining the presence of α-synuclein aggregates in the autopsied brains, and has been challenging in living subjects. Furthermore, disease-modifying therapeutic approaches to the pathogenetic pathways of α-synucleinopathies have been impeded by the lack of antemortem neuropathological investigations of the target protein lesions. Accordingly, imaging techniques capable of detecting α-synuclein aggregates with high sensitivity in the living human brain would provide definitive information on the

disease diagnosis at an early stage, and could be of great utility for the evaluation of efficacies yielded by candidate drugs targeting α-synuclein pathologies at nonclinical and subsequently clinical levels.

Molecular imaging modalities, as exemplified by positron emission tomography (PET), have enabled visualization of amyloid β (Klunk et al., 2004) and tau (Maruyama et al., 2013; Chien et al., 2014; Wong et al., 2018; Betthauser et al., 2019; Mueller et al., 2019; Sanabria Bohórquez et al., 2019; Tagai et al., 2020) deposits in the brain of living patients with Alzheimer's disease (AD) and allied disorders along with mouse models of these illnesses. A significant subset of the PET probes for these proteinopathies is a self-fluorescent β-sheet ligand and is applicable to intravital two-photon laser fluorescence microscopy of the animal models. Notably, the validity of the macroscopic PET technologies for capturing tau deposits has been proven by two-photon optical imaging of the tau transgenics at a microscopic level, demonstrating a rapid access of the probes to intraneuronal tau aggregates through the blood-brain barrier and neuronal plasma membrane in our previous works (Maruyama et al., 2013; Tagai et al., 2020). Hence, there has been growing expectation that small-molecule ligands for β-sheet structures would also serve as PET and optical probes for multi-scale assessments of intracellular α-synuclein fibrils. However, *in vivo* visualization of α-synuclein aggregates with high contrast have not been successful in the non-clinical and clinical settings. ^{11}C-BF-227, a PET ligand developed to detect amyloid β plaques (Kudo et al., 2007), has been reported to bind to α-synuclein lesions in the brains of MSA patients in a PET study (Kikuchi et al., 2010), but *in vitro* autoradiography of postmortem MSA brain sections in a more recent study did not support significant binding of ^{11}C-BF-227 to GCIs at concentrations typically achieved in PET experiments (Verdurand et al., 2018). The tau PET ligand, ^{11}C-PBB3 was also documented to react with α-synuclein lesions, including Lewy bodies, Lewy neurites, and GCIs, while it has been indicated that its binding affinity for α-synuclein pathologies is not sufficient for sensitive PET detection of these lesions in living individuals (Koga et al., 2017; Perez-Soriano et al., 2017). Indeed, PBB3 shows high affinity and selectivity for the β-sheet

structure of tau filaments, which is assumed to be ultrastructurally distinct from that of α-synuclein assemblies (Ono et al., 2017; Fitzpatrick et al., 2017; Goedert et al., 2018; Falcon et al., 2018; Guerrero-Ferreira et al., 2018 and 2019; Schweighauser et al., 2020). In the meantime, the modest reactivity of PBB3 with α-synuclein inclusions implies its utility as a starting material for the development of novel derivatives with more appropriate binding properties for *in vivo* imaging of α-synucleinopathies.

In our screening by *in vitro* evaluation, we found that derivatives of PBB3 with (*E*)-hex-2-en-4-yne linker, termed C05 series compounds, exhibited binding to α-synuclein pathologies with high reactivity and selectivity compared to PBB3 and BF-227. The *in vitro* characteristics of a chemical in this class, C05-01, were further analyzed with a tissue microarray in our latest work (Miranda-Azpiazu et al., 2020). In the present study, detailed non-clinical evaluations have revealed that another C05 compounds, C05-05, has more suitable properties than C05-01 for high-contrast detection of α-synuclein inclusions in murine and non-human primate models of propagating α-synuclein pathologies bimodally by *in vivo* optical and PET imaging from single-cell to brain-wide scales. Furthermore, the high binding affinity of C05-05 for α-synuclein inclusions in brain tissues derived from MSA and DLB cases has supported the applicability of this probe to clinical PET in humans.

RESULTS

C05 series compounds bind to α-synuclein inclusions *in vitro*

The tau PET ligand, PBB3, was found to have a moderate affinity for α-synuclein pathologies (Koga et al., 2017), which did not support the suitability of this compound for *in vivo* imaging of α-synucleinopathies. To develop novel ligands with higher reactivity with α-synuclein fibrils than PBB3 and BF-227, we screened PBB3 derivatives by fluorescence staining, in view of the fact that most of these chemicals are self-fluorescent (Maruyama et al., 2013; Ono et al., 2017). We then identified C05 series compounds, which possess an (*E*)-hex-2-en-4-yne

5

linker in the backbone structure, as candidates for α-synuclein imaging agents (Figure 1A). Double fluorescence staining of DLB brain slices with ligands and antibody against phosphorylated α-synuclein (pS129) demonstrated that C05-01, C05-03, and C05-05 strongly labeled Lewy bodies and Lewy neurites, whereas PBB3 and BF-227 yielded moderate and weak fluorescence signals, respectively, on these lesions (Figure 1B). To compare the binding selectivity for α-synuclein versus Aβ and tau pathologies between ligands, fluorescence staining of Lewy bodies and Lewy neurites in DLB amygdala and Aβ plaques and tau tangles in the AD middle frontal gyrus with the C05 series and reference compounds were quantified with a uniform imaging condition (Figure 1C and Figure S1). The background-corrected fluorescence intensity indicated that the signals attributed to C05-01, C05-03, and C05-05 bound to α-synuclein pathologies were significantly higher than those of Aβ and tau bound chemicals (Figure 1D), suggesting that the selectivity of C05 series compounds for α-synuclein versus Aβ and tau aggregates in the human brains. In contrast, the fluorescence signals originating from tau-bound PBB3 were significantly higher than those of this compound attached to α-synuclein and Aβ deposits, and the fluorescence signals attributed to Aβ-bound BF-227 were significantly higher than those of this compound attached to α-synuclein and tau deposits.

C05-05 enables *in vivo* optical visualization of α-synuclein inclusions in the brains of mice modeling propagating α-synucleinopathy

For assessing *in vivo* detectability of intracellular α-synuclein deposits by C05 series compounds at an individual cell level, we utilized a mouse model of propagating α-synuclein fibrillogenesis induced by inoculation of recombinant mouse α-synuclein fibrils into the brain parenchyma of a wild-type mouse (α-Syn mouse) (Masuda-Suzukake et al., 2013 and 2014). In the α-Syn mouse, aggregates of phosphorylated endogenous α-synuclein molecules resembling Lewy bodies and Lewy neurites emerged bilaterally in extensive brain regions, including the striatum, cortex, amygdala and substantia nigra, from 2 weeks after unilateral inoculation of α-synuclein fibrils into the striatum (Figure S2). Double-

staining of brain slices with fluorescent compounds and pS129 demonstrated that C05-01, C05-03, and C05-05 intensely labeled pS129-positive phosphorylated α-synuclein inclusions similar to Lewy bodies and Lewy neurites in the neocortex of α-Syn mice, while PBB3 and BF-227 modestly reacted with these deposits (Figure 1E). We selected C05-01 and C05-05 for the following characterizations in consideration of their suitability for ^{18}F radiolabeling towards wider availability.

To assess the time course of *in vivo* labeling of intraneuronal α-synuclein inclusions with C05-01 and C05-05 compared with PBB3, we conducted intravital two-photon laser fluorescence microscopy of the somatosensory cortex of an α-Syn mouse through a cranial window. Detection of C05-05, C05-01, and PBB3 signals in the same field of view of a single individual animal indicated rapid entry of C05-05 into the brain after intraperitoneal administration, reaching α-synuclein inclusions within 5 min, and the binding was sustained by 90 min (Figure 2). Unlike C05-05, no noticeable increases in fluorescence signals were produced in neurons by intraperitoneally injected C05-01 and PBB3. We did not employ BF-227 as a reference compound in these assays, as its fluorescence wavelength did not fit intravital observations. *Ex vivo* examination of frozen brain sections from α-Syn mouse following intravital two-photon microscopy further prove the binding of intraperitoneally administered C05-05 to α-synuclein inclusions abundantly present in the somatosensory cortex of this mouse (Figure S3).

Ex vivo examination of brain tissues collected from an α-Syn mouse at two hours after intraperitoneal BF-227 injection demonstrated no apparent interaction of this compound with α-synuclein inclusions stained with pS129 (Figure 3A and B). In contrast, brain samples collected from the α-Syn mouse at 90 min after intraperitoneal C05-05 injection contained numerous fibrillary inclusions labeled with the injected compound in broad areas of the brain, including the striatum, neocortex and amygdala, and these aggregates were subsequently stained with pS129, proving the entry of C05-05 into the brain followed by attachment of this ligand to intraneuronal α-synuclein assemblies (Figure 3C and D). *Ex vivo* examination of brain tissues collected from a wild-type control mouse injected with saline into the striatum showed no apparent distribution of intraperitoneally

7

administered BF-227 and C05-05 in the cerebral parenchyma (Figure S4). These *in vivo* and *ex vivo* data collectively demonstrate the capability of C05-05 for high-contrast optical visualization of α-synuclein inclusions in a living α-synucleinopathy model mouse.

In vivo microscopy with C05-05 allows tracking of pathological α-synuclein propagation through neural processes in the brain of a mouse model

To assess the dissemination of fibrillary α-synuclein pathologies via neuronal processes and cell bodies and consequent disruptions of these cellular structures on a longitudinal basis, we performed biweekly intravital two-photon imaging of α-synuclein inclusions in the brain of an α-Syn mouse inoculated with α-synuclein fibrils into the unilateral striatum. Prior to *in vivo* assessments, histopathological examinations of brain sections collected from α-Syn mice at several time points after the inoculation suggested the appearance of endogenous α-synuclein aggregates in neurites at two weeks, transient increase of inclusions in neurites and soma at four weeks, and subsequent decline of neuritic inclusions and maturation of somatic aggregates in the somatosensory cortex ipsilateral to the inoculation (Figure 4A).

Correspondingly, *in vivo* longitudinal microscopic imaging in α-Syn mice by two-photon laser scanning with C05-05 demonstrated the spatiotemporal changes of α-synuclein inclusions within an individual. Neuritic α-synuclein accumulations labeled with C05-05 appeared abundantly in the somatosensory cortex of the inoculated hemisphere at four weeks and then decreased at six weeks (Figure 4B, white arrowheads). Moreover, the formation and growth of somatic α-synuclein inclusions labeled with C05-05 were observed at 8 and 12 weeks after inoculation (Figure 4B, yellow arrowheads). High-magnification images clearly visualized the intraneuronal expansion of pathological α-synuclein aggregates from neuritic to somatic compartments in a week (Figure 4C). Moreover, time-course assays provided more compelling evidence for the disappearance of neuritic (Figure 4D, top) and somatic (Figure 4D, bottom) α-synuclein inclusions in two weeks and demonstrated loss of mCherry-expressing neurons bearing

C05-05-positive α-synuclein fibrils (Figure 4E). These *in vivo* data along the course after the inoculation of α-synuclein fibrils clarified stretching of α-synuclein depositions inside a single neuron, serially inducing neuritic and somatic fibril formations and subsequent breakdowns of neuronal structures, which is suggestive of α-synuclein-provoked neurotoxic insults. Our findings also demonstrated the utility of C05-05 as an optical probe for a dynamic pursuit of the neurodegenerative α-synuclein pathogenesis at a single-cell level.

PET imaging with ^{18}F-C05-05 visualizes depositions and propagations of pathological α-synuclein species in the brains of living model animals

To assess the *in vivo* performance of ^{18}F-labeled C05-05 (^{18}F-C05-05, Figure S5) as a PET ligand, we performed PET scans with ^{18}F-C05-05 for α-Syn mice at six months after injection of α-synuclein fibrils or saline into the bilateral striata, followed by *ex vivo* autoradiography and histopathological examinations. As depicted in Figure 5A, the retention of ^{18}F-C05-05 was overtly increased in the bilateral striatal and cortical areas of an α-Syn mouse, in sharp contrast to the low radio signals sustained in these brain regions of a control mouse. ^{18}F-C05-05 rapidly entered the brain after intravenous administration, and peak radioactivity uptakes estimated as standardized uptake values (SUVs) were 1.19 and 1.11 in the striatum and cortex, respectively (Figure 5B top). This was followed by a prompt washout of radioactivity from the brain of control mice, whereas the clearance was retarded in the striatum and cortex of α-Syn mice, reflecting radioligand binding to α-synuclein deposits. In the cerebellum lacking α-synuclein pathologies, there was no clear difference in the retention of ^{18}F-C05-05 between α-Syn and control mice (Figure 5A bottom and 5B top), justifying the use of the cerebellum as a reference tissue for quantification of the radioligand binding. The target-to-reference ratios of the radioactivity, which is denoted as standardized uptake value ratio (SUVR), at each time point and average SUVR at 90-120 min were increased in the striatum and cortex of α-Syn mice compared to those of control mice (Figure 5B bottom).

9

Ex vivo autoradiography of brain tissues collected from α-Syn and control mice used for PET scan at 90 min after intravenous ^{18}F-C05-05 injection demonstrated accumulation of the radioligand in the striatum, cortex and amygdala of the α-Syn mouse harboring abundant neuronal α-synuclein inclusions (Figure 5C and D). Conversely, there was no noticeable increase of ^{18}F-C05-05 retentions in these brain regions of the control mouse. In addition, the radioligand accumulation was minimal in the cerebellum of the α-Syn and control mice, the area devoid of α-synuclein deposits, while non-specific radioligand accumulations in several white matter regions, including the corpus callosum and fimbria of the hippocampus, was observed in both of these mice.

Since the small brain volumes of mice impeded clear separations between striatal and neocortical radio signals as assessed by PET, the *in vivo* traceability of the inter-regional α-synuclein dissemination with the use of ^{18}F-C05-05 remained rather inconclusive. We accordingly employed a non-human primate model of propagating α-synuclein pathologies by inoculating recombinant marmoset α-synuclein fibrils into the brain parenchyma (α-Syn marmoset). Our previous work documented that marmosets inoculated with murine α-synuclein fibrils displayed conversion of endogenous α-synuclein molecules into fibrillary aggregates, resulting in abundant accumulations of phosphorylated α-synuclein inclusions resembling Lewy bodies and Lewy neurites in the inoculation sites and subsequently remote brain areas through the neural network (Shimozawa et al., 2017). It was noteworthy that the retrograde propagation of pathological α-synuclein species from the caudate nucleus and putamen to substantia nigra through the nigrostriatal dopaminergic pathway was prominent at 3 months after inoculation (Shimozawa et al., 2017). Similar to this model, an α-Syn marmoset receiving marmoset α-synuclein fibrils exhibited enhanced retention of ^{18}F-C05-05 in a sub-portion of the caudate nucleus containing the injection site at 1 month after inoculation, which spread extensively in the caudate nucleus, putamen, and substantia nigra of the ipsilateral hemisphere and to a lesser extent in the contralateral left hemisphere at three months (Figure 6A). We also performed PET imaging of dopamine transporters with a specific radioligand, ^{11}C-PE2I,

10

which has proven useful for detecting degenerations of dopaminergic neurons in PD and its models (Innis et al., 1993; Scherfler et al., 2007; Ando et al., 2012), in the α-Syn marmoset before (Pre) and 3 months after inoculation. Parametric images of ^{11}C-PE2I binding potential (BP$_{ND}$) demonstrated a decrease of dopamine transpoters in the caudate nucleus, putamen, and substantia nigra of the inoculated hemisphere compared to the contralateral hemisphere, in agreement with the distribution of augmented ^{18}F-C05-05 retentions and pathological α-synuclein depositions (Figure 6B).

The brain of this animal was sampled at four months after inoculation, and immunohistochemical analyses of the brain slices demonstrated the distribution of pS129-stained α-synuclein inclusions in agreement with *in vivo* PET findings with ^{18}F-C05-05 PET at three months (Figure 6C). Double-staining with non-radiolabeled C05-05 and pS129 confirmed dense accumulations of α-synuclein aggregates in neuronal processes and somas recapitulating PD and DLB pathologies in the caudate nucleus, putamen, and substantia nigra of the inoculated hemisphere (Figure 6D). The corresponding brain areas of the contralateral hemisphere contained less abundant α-synuclein inclusions in neurites and neuronal somas. These α-synuclein pathologies were fluorescently labeled with non-radiolabeled C05-05, suggesting that the increased retention of ^{18}F-C05-05 in PET stemmed from its *in vivo* interaction with α-synuclein inclusions (Figure 6A and D). Meanwhile, non-specific accumulations of ^{18}F-C05-05 in bilateral white matter regions franking the putamen was noted in the pre-inoculation PET scan (Figure 6A), and the absence of α-synuclein deposits in these areas was ensured by histochemical and immunohistochemical assays.

These *in vivo* data provide the first PET demonstration of time-course imaging of pathological α-synuclein deposits in living animal models along the course of spatially expanding fibrillogenesis accompanied by the degeneration of neural circuits involved as dissemination pathways.

^{18}F-C05-05 displays high-affinity binding to α-synuclein pathologies in DLB and MSA brain tissues

To assess binding of ^{18}F-C05-05 to human α-synuclein pathologies at a low concentration (10 nM), we performed *in vitro* autoradiography of basal ganglia and amygdala sections from MSA and DLB cases, respectively (Figure 7A). The total binding of ^{18}F-C05-05 was markedly abolished by excessive non-radiolabeled C05-05, indicating the saturability of the radioligand binding. The MSA cases showed specific binding of ^{18}F-C05-05 in association with the local α-synuclein burden (Figure 7A and B). A case with mild pathology (MSA-1) had no binding of ^{18}F-C05-05 to the striatopallidal fibers. MSA-2, which was burdened with moderate α-synuclein deposits, showed weak ^{18}F-C05-05 radio signals in striatopallidal fibers containing numerous GCIs. MSA-3, which is a case with severe α-synuclein pathologies, exhibited intense radioligand binding to the striatopallidal fibers harboring densely packed GCIs. The DLB case also showed specific binding of ^{18}F-C05-05 in line with the distribution of α-synuclein pathology in the amygdala.

We then conducted triple staining of the sections used for autoradiography with non-radiolabeled C05-05 and antibodies against α-synuclein (LB509) and antibody against phosphorylated tau (pS199/202). The fluorescence labeling with non-radiolabeled C05-05 and LB509 was noted on GCIs in the MSA striatopallidal fibers, and Lewy bodies and Lewy neurites in the DLB amygdala and these areas were devoid of pS199/202-immunoreactive phosphorylated tau pathologies (Figure 7B).

In vitro autoradiography was also carried out using brain slices of the α-Syn marmoset showing enhanced retentions of ^{18}F-C05-05 in the brain area enriched with α-synuclein deposits in PET scans (Figure 6A-C). We found no marked difference in the autoradiographic signals of ^{18}F-C05-05 between the substantia nigra heavily burdened with α-synuclein aggregates and prerubral fields lacking pathologies (Figure 7A and B). As the binding of ^{18}F-C05-05 to the α-Syn marmoset lesions was less than its binding to moderate-grade GCIs in MSA-2 but still yielded detectable radio signals in PET measurements, it is likely that ^{18}F-

C05-05-PET would capture α-synuclein fibrils with relatively low abundance and packing maturity comparable to the marmoset model.

We also quantified the affinity of ^{18}F-C05-05 for α-synuclein aggregates in homogenized DLB amygdala tissues in comparison to AD frontal cortical tissues. Radioligand binding in these tissues was homologously blocked by non-radiolabeled C05-05 in a concentration-dependent fashion (Figure 7C), indicating binding saturability. ^{18}F-C05-05 displayed high-affinity binding in DLB homogenates with the concentration inducing 50% homologous inhibition (IC50) of 1.5 nM (Figure 7F). This radioligand was not highly reactive with Aβ and tau aggregates in AD tissues relative to DLB α-synuclein deposits, with IC50 of 12.9 nM. Unlike ^{18}F-C05-05, tau PET tracers, ^{11}C-PBB3 and ^{18}F-PM-PBB3, displayed relatively low affinities for α-synuclein deposits in DLB homogenates with IC50 values of 58.8 nM and 26.5 nM, respectively, while these radioligands more tightly bound to AD-type protein fibrils than α-synuclein aggregates, with IC50 values of 8.6 nM and 8.0 nM, respectively (Figure 7F). These results of *in vitro* autoradiographic and radioligand binding assays highlight the reactivity of ^{18}F-C05-05 with human α-synuclein pathologies with much higher affinity than existing PET tracer for non-α-synuclein aggregates, supporting the potentials of this novel radioligand for visualizing hallmark lesions in living patients with α-synucleinopathies.

DISCUSSION

The current work has offered a powerful imaging tool to pursue the molecular and cellular mechanisms of the neurodegenerative α-synucleinopathies in the basic research on animal models, and this technology is translatable to clinical PET assessments of PD and associated disorders. Indeed, the first-in-human study of ^{18}F-C05-05 is being prepared by undertaking safety tests of this compound. The imaging methodology with ^{18}F-C05-05 potentially meets the needs for the early diagnosis and differentiation of neurocognitive and movement disorders by targeting neurotoxic fibrillary species of α-synuclein molecules,

13

along with the discovery and development of anti-α-synuclein therapeutics as disease-modifying treatments (Adler et al., 2014; Joutsa et al., 2014; Wong et al., 2017; Brundin et al., 2017). Our bimodal *in vivo* optical and PET assays have allowed longitudinal tracking of α-synuclein propagations through neural pathways from subcellular to brain-wide scales, facilitating the non-clinical evaluation of efficacies exerted by a candidate drug counteracting the etiological processes of α-synucleinopathies.

It is noteworthy that the substitution of the (*2E*, *4E*)-hexa-2, 4-dien linker in the chemical structure of a tau imaging agent, PBB3, with (*E*)-hex-2-en-4-yne resulted in a profound increase of the ligand binding to α-synuclein versus tau and Aβ fibrils, leading to the generation of C05 series compounds. A recent molecular docking analysis based on the cryo-EM structure of AD-type tau filaments suggested that PBB3 binds to these fibrillary assemblies in a direction perpendicular to the fibril axis (Goedert et al., 2018). A more recent cryo-EM assay revealed that the protofilament axis tilts with respect to the fibril axis in α-synuclein assemblies extracted from MSA brains (Schweighauser et al., 2020). The linker substitution could produce differences in the backbone twist angle between PBB3 and C05 series compounds at a minimum energy state, which may affect the fitness of the chemical for the binding surface on the filament with a unique distortion angle. In fact, IC50 of C05-05 for the homologous binding blockade was approximately 40- and 18-fold smaller than those of PBB3 and PM-PBB3, respectively, implying the critical role of the linker angle in the ligand affinity for pathological fibrils. It is yet to be clarified whether C05 series compounds exhibit differential reactivity with DLB and MSA α-synuclein fibrils, although autoradiographic labeling of pathological inclusions in both illnesses was demonstrated with ^{18}F-C05-05 in the present assay. It has been reported that the ultrastructure of tau fibrils show diversity among AD, Pick's disease, and corticobasal degeneration (Fitzpatrick et al., 2017; Falcon et al., 2018; Zhang et al., 2020), and this variation could underly distinct binding of tau PET probes to AD versus non-AD tau pathologies (Ono et al., 2017; Tagai et al., 2020). On the analogy of these insights, it will be required to assess the *in vitro* interaction of

14

C05-05 and related chemicals with aggregates in various α-synucleinopathies, which will provide useful information for predicting the *in vivo* performance of the probes in clinical PET imaging of cases with these disorders.

Intravital two-photon laser microscopy with C05-05 has enabled longitudinal imaging of the α-synuclein fibrillogenesis at a subcellular scale in the brain of a living α-synucleinopathy mouse model for the first time, visualizing the dynamic processes in the formation of α-synuclein lesions, including a spatiotemporal connection between the developments of Lewy neurite-like neuritic aggregates and Lewy body-like somatic inclusion in a single neuron, as well as the disappearance of these fibrillar deposits. While we found evidence that the vanishment of α-synuclein fibrils reflects the loss of neurons loaded with inclusions, the dynamic appearance and disappearance of the aggregates may also unfold as a consequence of continuous translocations of α-synuclein assemblies through neuritic processes. The mechanisms linking the accumulations of α-synuclein fibrils and loss of neurons or their substructures remain elusive, and cell-autonomous (Desplats et al., 2009; Ordonez et al., 2018) and non-cell-autonomous (Kim et al., 2014; Gordon et al., 2018) death of neurons could be provoked in the pathogenetic pathway. Such etiological cellular events will be microscopically examined by monitoring interactions between glial cells expressing fluorescent proteins and neurons bearing C05-05-positive α-synuclein deposits. Meanwhile, the transient accumulation of α-synuclein aggregates in neuronal compartments may indicate the transport of these pathological components along neurites, but it is also presumable that a significant portion of the fibrils could be degraded by autophagic and other related processes. In addition, the stretching of α-synuclein depositions inside neurites towards the cell body might be caused by a domino-like conversion of endogenous α-synuclein molecules to misfolded forms prone to the self-aggregation, whereas dislocation of native α-synuclein proteins from presynaptic to neuritic and somatic compartments should be necessary for this involvement. The localization of endogenous α-synuclein molecules and their engagement in the fibril formation would be investigated in detail by expressing fused α-synuclein

15

and fluorescent proteins (Yang et al., 2010) in neurons of α-Syn mice, which could be used for intravital microscopic assays with C05-05.

Since our longitudinal PET scans with ^{18}F-C05-05 have successfully captured the dissemination of α-synuclein pathologies in an α-Syn marmoset along the course following the fibril inoculation, this imaging technology will pave the way to the neuroimaging-based evaluations of the disease severity and progression in α-synucleinopathy patients. The topology of α-synuclein pathology and its chronological change are known to be closely correlated with the symptomatic phenotypes (Braak et al., 2003; Saito et al., 2003; Henderson et al., 2019), indicating the local neurotoxicity of aggregated α-synuclein molecules. In the marmoset model of α-synuclein propagation, intensification and expansion of α-synuclein depositions visualized by ^{18}F-C05-05 were in association with declines of the nigral dopaminergic neurons and their striatal terminals as assessed by PET imaging of dopamine transporters, in resemblance to the dopaminergic deficits in PD. This observation also implies that ^{8}F-C05-05 could illuminate α-synuclein species critically involved in functional and structural disruptions of neurons. Previous studies suggested linkage of misfolded α-synuclein proteins with synaptic dysfunctions, such as a decrease of soluble N-ethylmaleimide-sensitive factor attachment protein receptor complex assembly and synaptic vesicle motility (Nemani et al., 2010; Scott et al., 2012; Choi et al., 2013; Wang et al., 2014). Influences of C05-05-detectable α-synuclein accumulations on the functionality of individual neurons will be examined by conducting intravital two-photon microscopy of α-Syn mice expressing calcium sensor proteins, and this assay system would be utilized for obtaining pathological and functional outcome measures in the non-clinical evaluation of a candidate therapeutic agent.

The total amount of abnormal α-synuclein proteins was reported to be approximately 50 - 200 nM in the brainstem and subcortical regions of advanced DLB and MSA cases, which was more than 10-fold smaller than the amount of Aβ peptide deposited in the brain of AD patients (Deramecourt et al., 2006). This finding raises a concern on the visibility of α-synuclein pathologies by PET in a clinical setting. The sensitive detection of α-synuclein pathologies in the brain of

16

murine and non-human primate models was permitted by appropriate pharmacokinetic and pharmacodynamic characteristics of this probe in living animals. The high reactivity of C05 series compounds with α-synuclein inclusions relative to Aβ and tau deposits was demonstrated by *in vitro* fluorescence staining and binding assays, and IC50 of ^{18}F-C05-05 for the homologous blockade of its binding to α-synuclein aggregates in DLB tissue was 5 – 6 times lower than those of ^{11}C-PBB3 and ^{18}F-PM-PBB3 for the self-blockade of their binding to tau fibrils in AD tissue. Accordingly, PET with ^{18}F-C05-05 would visualize α-synuclein depositions in DLB cases even if the brains of these patients possess radioligand binding sites with 5-fold lower density than AD brains. In contrast, IC50 values of ^{11}C-PBB3 and ^{18}F-PM-PBB3 for the self-blockade of their binding in DLB brain homogenates were much higher than that of ^{18}F-C05-05, leading to the notion that these tau ligands are unlikely to detect α-synuclein fibrils in living individuals with sufficient sensitivity. Furthermore, our autoradiographic data illustrated that α-synuclein pathologies in the midbrain of an α-Syn marmoset were less abundant than pathological deposits in the DLB amygdala, but these non-human primate deposits were detectable by ^{18}F-C05-05-PET. These facts could bring an implication on the usability of ^{18}F-C05-05 for high-sensitivity imaging of core pathologies in α-synucleinopathy cases.

In addition to the reactivity with the target lesion, the entry of the compound into the brain is a key factor for yielding a high signal-to-noise ratio in PET neuroimaging. Among C05 series compounds, C05-01 and C05-05 were fluorinated chemicals with desirable *in vitro* binding properties (Miranda-Azpiazu et al., 2020; Figure 1D). However, visualization of α-synuclein aggregates by intravital two-photon microscopic imaging of model mice was unsuccessful with C05-01. It is conceivable that the hydroxy moiety of C05-01 could be promptly conjugated with sulfate after systemic administration in a mode similar to PBB3 (Hashimoto et al., 2014), and such metabolic modification was circumvented by the replacement of this structural group with a fluoroisopropanol moiety in PM-PBB3 (Tagai et al., 2020) and C05-05, enhancing the uptake of the intact compound into the brain. In fact, the peak radioactivity uptake of ^{18}F-C05-05 in

the frontal cortex (SUV, 1.11; Figure 5B) was approximately 2-fold higher than that of ^{18}F-C05-01 (SUV, 0.58; Figure S6) in PET imaging of wild-type control mice.

Despite promising features of ^{18}F-C05-05-PET as a neuroimaging technique translatable from animal models to humans, several technical issues are yet to be addressed. In α-Syn mice, PET with ^{18}F-C05-05 visualized abundant α-synuclein accumulation in the striatum and cortex, but failed to detect abundant α-synuclein accumulation in amygdala (Figure S7). *Ex vivo* examination of brain tissues collected from the model mice confirmed the binding of ^{18}F-C05-05 systemically administered to α-synuclein inclusions deposited in this area. Therefore, the incapability of ^{18}F-C05-05-PET for capturing target pathologies in the amygdala is attributable to the limited spatial resolution of the imaging device and consequent partial volume effects, which might preclude *in vivo* neuropathological assessments in a relatively small anatomical structure. A possible solution to this issue could be the use of a non-human primate model with a larger brain volume, but it should be taken into account that non-specific accumulation of ^{18}F-C05-05 in white matter regions was observed by PET imaging of a marmoset model even before inoculation of α-synuclein fibrils. Notwithstanding these pathology-unrelated signals, ^{18}F-C05-05-PET could detect increased radioligand retention associated with α-synuclein inclusions in white matter structures. In the clinical application of ^{18}F-C05-05 to humans, non-specific radio signals in the white matter might impede high-contrast imaging of α-synuclein lesions, particularly in the MSA brains, since GCIs accumulates in white matter areas such as deep cerebellar structures (Wakabayashi et al., 1998b; Dickson et al., 1999). Moreover, several tau PET ligands are known to show off-target binding to monoamine oxidases A and B (Harada et al., 2017; Ng et al., 2017; Lemoine et al., 2018; Vermeiren et al., 2017). Although previous studies documented that ^{11}C-PBB3 and its analogs, including ^{18}F-PM-PBB3 and ^{18}F-C05-01, did not cross-react with these enzymes (Ni et al., 2018; Tagai et al., 2020; Miranda-Azpiazu et al., 2020), the insensitivity of ^{18}F-C0-05 to monoamine

oxidases will need to be directly examined by either *in vitro* or *in vivo* blockade experiments.

In the present study, we granted the highest priority to the sensitive PET detection of α-synuclein pathologies with a high-affinity radioligand, as such a goal has been reached in neither animal models nor humans. In the brains of α-synucleinopathy patients, α-synuclein lesions are often co-localized with Aβ and tau aggregates. Tau pathologies at Braak stage III or above and Aβ pathologies are observed in more than 50% and 80% of α-synucleinopathy patients, respectively (Irwin et al., 2017). This fact raises the necessity for the development of a specific ligand for α-synuclein deposits with minimal cross-reactivity with other pathological fibrils. ^{18}F-C05-05 displayed more than eight times smaller IC50 (1.5 nM) in DLB homogenates than in AD homogenates (12.9 nM), but its reactivity with tau deposits might not be markedly lower than that of ^{11}C-PBB3 and ^{18}F-PM-PBB3. In view of the putative structure-activity relationships indicated in this study, however, we are able to take advantage of β-sheet ligands with the (*E*)-hex-2-en-4-yne linker as potent binders, and structural modifications will be made for enhancing the selectivity of the chemicals by replacing aromatic rings and sidechains. It is also of significance that optical and PET imaging modalities can be utilized for the characterization of new candidate imaging agents.

To conclude, the current neuroimaging platform incorporating C05-05 is implementable for multi-scale analysis of the neurodegenerative α-synuclein fibrillogenesis and pharmacological actions of a drug candidate on this etiological process in animal models. Our assays have also provided essential information on the feasibility of ^{18}F-C05-05 for the first demonstration of α-synuclein PET imaging in humans with adequate contrast.

ACKNOWLEDGEMENTS

AUTHOR CONTRIBUTIONS

Conceptualization, M.O. and M.Higuchi; Formal Analysis, M.O., M.T., M.F., Y.N., and K.M.; Investigation, M.O., M.T., M.F., W.M., Y.N., K.M., T.Minamihisamatsu, S.U., and Y.Takado; Resources, M.Hasegawa, A.S., M.S., and H.T.; Visualization, M.O., M.T., Y.N., K.M., and S.U.; Supervision, N.S., M.-R.Z., T.Minamimoto, M.Hasegawa, and M.Higuchi; Project Administration, M.Higuchi; Funding Acquisition, M.O., and M.Higuchi; Critical Review and Editing of the Manuscript, all authors.

DECLARATION OF INTERESTS

M.O., M.-R.Z., and M.Higuchi filed a patent on compounds related to the present report (2019-034997, PCT/JP2020/002607).

FIGURE LEGENDS

Figure 1. C05 series compounds bind to α-synuclein inclusions in DLB and mouse model of α-synucleinopathy *in vitro*.

(**A**) Chemical structures of C05 series compounds, PBB3 and BF-227. C05-01, C05-03, and C05-05 are derivatives from PBB3 with the substitution of its (2*E*,4*E*)-hexa-2,4-diene linker (blue) with (*E*)-hex-2-en-4-yne (red). (**B**) Double fluorescence staining of Lewy bodies (arrows) and Lewy neurites (arrowheads) in the amygdala sections of a patient with DLB (also see Table S1) with 30 µM of self-fluorescent ligands (left) and anti-phosphorylated α-synuclein antibody, pS129 (right). C05-01, C05-03, and C05-05 intensely labeled α-synuclein inclusions in DLB brain sections, while PBB3 and BF-227 yielded moderate and weak staining of these lesions, respectively. (**C**) Fluorescence microscopic images of various fibrillary protein pathologies, including Lewy bodies and Lewy neurites in the amygdala sections of a patient with DLB (left) and amyloid plaques (right, arrows) and neurofibrillary tangles (right, arrowheads) in the middle frontal gyrus sections of a patient with AD (AD-1, also see Table S1), labeled with C05-01, C05-03, C05-05, PBB3, and BF-227 were taken under a uniform imaging condition. (**D**) Fluorescence signal intensities in Lewy bodies and neurites (black), amyloid plaques (gray), and neurofibrillary tangles (white) in the images illustrated in **C** were normalized according to background signals. Quantification of the background-corrected fluorescence intensity indicated that C05-01 ($F_{(2, 74)}$ = 6.729, p = 0.0021), C05-03 ($F_{(2, 73)}$ = 9.151, p = 0.0003), and C05-05 ($F_{(2, 85)}$ = 36.92, $p < 0.0001$) bound to α-synuclein pathologies produced significantly more intense signals than these chemicals bound to Aβ and tau pathologies. In contrast, PBB3 bound to tau pathologies elicited stronger fluorescence than this compound bound to α-synuclein and Aβ pathologies ($F_{(2, 73)}$ = 12.57, $p < 0.0001$), and the fluorescence signals attributed to BF-227 bound to Aβ pathologies were significantly more intense than the signals related to α-synuclein- and tau-bound BF-227 ($F_{(2, 63)}$ = 114.0, $p < 0.0001$). Data are presented as mean ± SD. *, $p < 0.05$; **, $p < 0.01$; ***, $p < 0.001$; ****, $p < 0.0001$ by one-way ANOVA with post-hoc Tukey's HSD test. (**E**) Double fluorescence staining of α-synuclein inclusions

21

resembling Lewy bodies (left) and Lewy neurites (right) in the neocortical sections of an α-Syn mouse injected with α-synuclein fibrils into the unilateral striatum (10 weeks after inoculation) with 30 µM of self-fluorescent ligands (top) and pS129 (bottom). Scale bars, 20 µm (**B**, **C**, and **E**).

Figure 2. C05-05 enables *in vivo* optical visualization of individual α-synuclein inclusions in the brain of an α-Syn mouse model.

Maximum intensity projection of fluorescence signals in an identical 3D volume (field of view, 150 × 150 µm; depth, 25 - 100 µm from the brain surface) of the somatosensory cortex of a living α-Syn mouse at 8 – 10 weeks after inoculation of α-synuclein fibrils into the neocortex. Exogenous α-synuclein fibrils were found to vanish by 2 weeks after injection, followed by aggregation of endogenous α-synuclein molecules. From left, images acquired before (Pre) and 5, 30, 60 and 90 min after intraperitoneal administration of C05-05 (1.66 mg/kg) (top), C05-01 (1.66 mg/kg) (middle), and PBB3 (1.66 mg/kg) (bottom) are displayed. Cerebral blood vessels were labeled in red with intraperitoneally administered sulforhodamine 101. Somatodendritic labeling of putative neurons with C05-05 was observed as green fluorescence from 5 min after ligand administration. Fluorescence images of the corresponding area at 5 - 90 min after C05-01 and PBB3 injections demonstrated no overt retention of the tracer in the tissue.

Figure 3. C05-05 enables *ex vivo* detection of α-synuclein inclusions in the brain of an α-synucleinopathy mouse model.

(**A**) *Ex vivo* examination of frozen brain sections from an α-Syn mouse at 10 weeks after the inoculation of α-synuclein fibrils into the right striatum. The brain tissue was collected at 2 hours after intraperitoneal administration of BF-227 (1.66 mg/kg). Distributions of systemically injected BF-227 in coronal brain sections (top) and postmortem immunolabeling of adjacent sections with pS129 (bottom) at bregma +2.22, +0.50, -0.46, -1.94, and -3.16 mm are displayed. (**B**) Medium-power (left) and high-power (right) photomicrographs of cortical sections shown in **A**. *Ex vivo* examination revealed that α-synuclein inclusions were devoid

of labeling with intraperitoneally administered BF-227. (**C**) *Ex vivo* examination of frozen brain sections from an α-Syn mouse at 8 weeks after the inoculation of α-synuclein fibrils into the right striatum. The brain tissue was collected at 90 min after intraperitoneal administration of C05-05 (1.66 mg/kg). Distributions of systemically injected C05-05 in coronal brain sections (top) and immunolabeling of adjacent brain sections with pS129 (bottom) at bregma +2.22, +0.50, -0.46, -1.94 and -3.16 mm are displayed. (**D**) Medium-power (left) and high-power (right) photomicrographs of cortical sections shown in **C**. Individual α-synuclein inclusions were found to be intensely labeled with intraperitoneally administered C05-05. Scale bars, 50 μm (**B** and **D**).

Figure 4. Pathological α-synuclein propagates to extensive brain areas with a transient oscillation of the aggregate amount in the brains of a living α-Syn mouse model.

(**A**) Distribution of phosphorylated α-synuclein immunostained with pS129 in coronal brain sections at bregma -1.94 of α-Syn mice at 1, 2, 4, 6, and 8 weeks after inoculation of α-synuclein fibrils into the right striatum (top), and high-power photomicrographs of the ipsilateral somatosensory cortex (bottom). Scale bars, 50 μm. (**B**) Longitudinal *in vivo* two-photon microscopic imaging of α-synuclein inclusions with systemically administered C05-05 in the right somatosensory cortex of a single indivisual α-Syn mouse at 2, 4, 6, 8, and 12 weeks after inoculation of α-synuclein fibrils into the right striatum. A maximum projection of fluorescence in an identical 3D volume (field of view, 182 × 182 μm; depth, 40 - 400 μm from the brain surface) at 90 min after intraperitoneal administration of C05-05 demonstrated propagation of C05-05-positive α-synuclein inclusions to the cortical area from 4 weeks after the intrastriatal fibril inoculation, and subsequent changes in the subcellular location and amount of the inclusions. White arrowheads indicate neuritic α-synuclein accumulations which disappeared from 4 to 6 weeks after the fibril inoculation, and yellow arrowheads indicate somatic α-synuclein inclusions which appeared from 8 weeks after the fibril inoculation. (**C**-**E**) Longitudinal intravital microscopy of the somatosensory

23

cortex (field of view, 55 × 55 μm; depth, 0 - 75 μm from the brain surface) of an α-Syn mouse demonstrated extension of a C05-05-positive intraneuronal α-synuclein inclusion from neurite to soma in a week (**C**, arrowheads), and disappearance of C05-05-positive (green) neuritic inclusion similar to Lewy neurite (**D**, top, arrowheads) and somatic deposit resembling Lewy body (**D**, bottom, arrowheads) like inclusions in two weeks, along with loss of a mCherry-expressing (red) neuron bearing a C05-05-positive (green) inclusion (**E**, arrowheads) in three weeks. Cerebral blood vessels were also labeled in red with intraperitoneally administered sulforhodamine 101 (**B**-**E**).

Figure 5. *In vivo* PET imaging with ^{18}F-C05-05 detects α-synuclein deposits in the brains of α-Syn mice.

(**A**) Coronal PET images at bregma +0.50 mm (top) and -0.46 mm (middle) containing the striatum and neocortex, and -6.64 mm (bottom) containing the cerebellum generated by averaging dynamic scan data at 60 - 90 min after intravenous administration of ^{18}F-C05-05 (30.8 ± 0.4 MBq) in mice at 6 months after inoculation of α-synuclein fibrils (α-Syn mouse, left) or saline (control mouse, right) into the bilateral striata. PET images are superimposed on an MRI template. Voxel values represent SUV. (**B**) Time-radioactivity curves in the striatum, neocortex, and cerebellum during the dynamic PET scan (top), time-course changes in the target-to-cerebellum ratio of radioactivity (SUVR, left and middle panels in bottom row), and the average of target-to-cerebellum ratios at 90 - 120 min (bottom, right) in α-Syn (red symbols) and control (black symbols) mice. There were significant main effects of animal group and region in two-way, repeated-measures ANOVA (group, $F_{(1, 6)} = 11.39$, $p = 0.015$; region, $F_{(1, 6)} = 111.9$, $p < 0.0001$). *, $p < 0.05$ by Bonferroni's post hoc test. Data are presented as mean (top) or mean ± SEM (bottom) in four α-Syn or control mice. (**C**) *Ex vivo* examination of frozen brain sections obtained from α-Syn (top) and control (bottom) mice after PET imaging to assess distributions of intravenously administered ^{18}F-C05-05 (27.8 ± 0.2 MBq), in comparison with immunolabeling of the same sections with pS129. From left, coronal brain sections at bregma

+0.50, -0.46, -1.94, and -6.64 mm are displayed. (**D**) High-power photomicrographs showing double fluorescence staining of the section used for *ex vivo* examination with 30 µM of unlabeled C05-05 (top) and pS129 (bottom). Areas correspond to those indicated by arrowheads in C. The striatum (**1**), somatosensory cortex (**4**), and amygdala (**5**) of an α-Syn mouse contained abundant α-synuclein inclusions. The corpus callosum (**2**) and fimbria of the hippocampus (**3**) showed a small number of α-synuclein deposits. The cerebellum (**6**) contained very few α-synuclein inclusions. Scale bars, 100 µm.

Figure 6. Longitudinal *in vivo* PET imaging with ^{18}F-C05-05 visualizes the propagation of pathological α-synuclein aggregates in the brain of an α-Syn marmoset.

(**A**) Coronal brain images in a marmoset injected with α-synuclein fibrils and saline into the right and left caudate nucleus and putamen, respectively, generated by averaging dynamic PET data at 30 - 120 min after intravenous administration of ^{18}F-C05-05 (89.6 ± 15.3 MBq) (also see Figure S8). Images were acquired before (Pre), and 1 and 3 months after the fibril inoculation, and white and blue asterisks indicate the sites of α-synuclein fibril and saline injections, respectively. Brain volume data were sectioned at 9.5 mm (left) and 5.0 mm (right) anterior to the interaural line to generate images containing the caudate nucleus/putamen and caudate nucleus/putamen/substantia nigra, respectively. PET images are superimposed on an MRI template, and voxel values represent SUV. Longitudinal ^{18}F-C05-05 PET showed the expansion of radio signals from a part of the right caudate nucleus to extensive brain areas, including bilateral regions of the caudate nucleus, putamen, and substantia nigra from 1 to 3 months after inoculation. (**B**) Parametric images of BP_{ND} for ^{11}C-PE2I (radioactivity dose: 89.2 ± 2.0 MBq) in a single individual α-Syn marmoset demonstrated reduction of the radioligand binding in the right caudate nucleus, putamen, and substantia nigra at 3 months after inoculation compared to the baseline before inoculation (Pre). Brain volume data were sectioned at 9.5 mm (left) and 5.0 mm (right) anterior to the interaural line, and BP_{ND} images were superimposed on an MRI

template. (**C**) Histopathological assays were carried out 1 month after the final PET scan, demonstrating a similarity between the regional distributions of α-synuclein inclusions stained with pS129 and localization of ^{18}F-C05-05 retentions in PET images at 3 months. (**D**) High-power photomicrographs showing fluorescence staining of brain sections shown in B with pS129 and adjacent brain sections with 30 μM of non-radiolabeled C05-05. Areas correspond to those indicated by arrowheads in **B**. The right caudate nucleus (**2** and **6**), putamen (**4** and **8**), and substantia nigra (**10**) contained highly abundant α-synuclein inclusions. The left caudate nucleus (**1** and **5**) and putamen (**3** and **7**) contained moderate amounts of α-synuclein deposits, and the left substantia nigra (**9**) contained sparse α-synuclein inclusions. Scale bars, 50 μm.

Figure 7. ^{18}F-C05-05 displays high-affinity binding to α-synuclein pathologies in DLB and MSA brain tissues.

(**A** and **B**) Autoradiographic labeling of sections, including the basal ganglia derived from patients with MSA (MSA-1, 2, and 3, also see Table S1), amygdala derived from patients with DLB, and substantia nigra (SN) and prerubral field (PRF) derived from an α-Syn marmoset, with 10 nM of ^{18}F-C05-05 in the absence (**A**, left) and presence (**A**, right) of 10 μM of non-radiolabeled C05-05, and high-power photomicrographs showing triple fluorescence staining of the section used for ^{18}F-C05-05 autoradiography with 30 μM of non-radiolabeled C05-05, LB509, and pS199/202 (**B**). Areas in **B** correspond to locations indicated by arrowheads in **A**. No overt specific binding of ^{18}F-C05-05 was detected in the striatopallidal fibers (**1**) of MSA-1 with mild pathology, weak but clearly noticeable radioligand binding to these fibers (**3**) was seen in MSA-2 with moderate pathology, and strong radioligand binding to the same subregion (**5**) was observed in MSA-3 with severe pathology. No significant binding of ^{18}F-C05-05 was shown in the areas devoid of α-synuclein pathologies in MSA cases (**2**, **4**, and **6**). In the amygdala of a DLB case, strong binding of ^{18}F-C05-05 was seen in an area harboring abundant Lewy bodies and Lewy neurites (**7**). In contrast, no significant binding of ^{18}F-C05-05 was noted in an area with a very small amount of α-synuclein

26

pathologies (**8**). In addition, no specific binding of ^{18}F-C05-05 was detected in SN (**9**) and PRF (**10**) of an α-Syn marmoset. Immunohistochemistry with pS199/202 indicated the absence of tau deposits in these regions. Scale bars, 100 µm. (**C-E**) Total (specific + non-specific) binding of ^{18}F-C05-05 (**C**), ^{11}C-PBB3 (**D**), and ^{18}F-PM-PBB3 (**E**) in the DLB amygdala (black squares, also see Table S1) and AD frontal cortex (grey triangles, AD-2, also see Table S1) samples homologously blocked by non-radiolabeled C05-05, PBB3, and PM-PBB3, respectively, with varying concentrations. Data are presented as mean ± SD in four samples and are expressed as % of average total binding. (**F**) Homologous blockades of ^{18}F-C05-05, ^{11}C-PBB3, and ^{18}F-PM-PBB3 binding described by a one-site model and parameters resulting from curve fits.

STAR⋆METHODS:

KEY RESOURCES TABLE

REAGENT or RESOURCE	SOURCE	IDENTIFIER
Antibodies		
pS129	Abcam	Cat.#:ab59264; RRID:AB_2270761
LB509	Abcam	Cat.#:ab27766; RRID:AB_727020
AT8	ThermoFisher Scientific	Cat.#:MN1020; RRID:AB_223647
6E10	BioLegend	Cat.#:803004; RRID:AB_2715854
pS199/202	ThermoFisher Scientific	Cat.#:44-768G; RRID:AB_2533749
Chemicals, Peptides, and Recombinant Proteins		
^{18}F-C05-05	This paper	N/A
^{11}C-PBB3	Maruyama et al., 2013	N/A
^{18}F-PM-PBB3	Tagai et al., 2020	N/A
^{11}C-PE2I	Ando et al., 2012	N/A
^{18}F-C05-01	Miranda-Azpiazu et al., 2020	N/A
C05-03	This paper	N/A
BF-227	Nard Institute	Cat. #: NP039-0
sulforhodamine 101	Sigma-Aldrich	Cat. #: S7635
Recombinant mouse wild-type α-synuclein and fibrils	Masuda-Suzukake et al., 2014	N/A
Recombinant marmoset wild-type α-synuclein and fibrils	This paper	N/A
Bacterial and Virus Strains		
AAV-Syn-mCherry	Nagai et al., 2020	N/A
Experimental Models: Organisms/Strains		
α-Syn mouse	Masuda-Suzukake et al., 2014	N/A

α-Syn marmoset	this paper	N/A
Biological Samples		
Table S1	this paper	N/A
Software and Algorithms		
Prism	Graph Pad	https://www.graphpad.com/scientific-software/prism/
PMOD	PMOD Technologies	https://www.pmod.com/web/
ImageJ (FIJI)	NIH	https://fiji.sc/

RESOURCE AVAILABILITY

Lead Contact

Further information and requests for resources and reagents should be directed to the Lead Contact, Maiko Ono (ono.maiko@qst.go.jp)

EXPERIMENTAL MODEL AND SUBJECT DETAILS

Experimental animals

All animals studied here were maintained and handled in accordance with the National Research Council's Guide for the Care and Use of Laboratory Animals. Protocols for the present animal experiments were approved by the Animal Ethics Committees of the National Institutes for Quantum and Radiological Science and Technology (approval number: 07-1049-31, 11-1038-11). A total of 35 adult C57BL/6J mice (male, mean age 5.4 months, Japan SLC Inc) were used for the histochemical analysis, *ex vivo* examination, two-photon microscopy and PET scanning, and one adult marmoset (male, 2 years old, 300-365 g body weights) was used for PET scanning and histochemical analysis in this study. All mice and the marmoset were maintained in a 12 hours' light/dark cycle with ad libitum access to standard diet and water.

29

METHOD DETAILS

Compounds and antibodies

C05-01 ((*E*)-2-(4-(2-fluoro-6-(methylamino)pyridine-3-yl)but-1-en-3-yn-1-yl)benzo[*d*]thiazol-6-ol), C05-03 ((*E*)-2-(4-(6-(methylamino)pyridin-3-yl)but-1-en-3-yn-1-yl)benzo[*d*]thiazol-6-ol), C05-05 ((*E*)-1-fluoro-3-((2-(4-(6-(methylamino)pyridine-3-yl)but-1-en-3-yn-1-yl)benzo[*d*]thiazol-6-yl)oxy)propan-2-ol), PBB3 (2-((1*E*,3*E*)-4-(6-(methylamino)pyridine-3-yl)buta-1,3-dienyl)benzo[*d*]thiazol-6-ol), desmethyl precursor of ^{11}C-PBB3, PM-PBB3 1-fluoro-3-((2-((1*E*,3*E*)-4-(6-(methylamino)pyridine-3-yl)buta-1,3-dien-1-yl)benzo[*d*]thiazol-6-yl)oxy)propan-2-ol, tosylate precursor of ^{18}F-PM-PBB3 and desmethyl precursor of ^{11}C-PE2I were custom-synthesized (Nard Institute and KNC Laboratories). BF-227 (Nard Institute, NP039-0) and sulforhodamine 101 (Sigma, S7635) are commercially available. Monoclonal antibodies against α-synuclein phosphorylated at Ser 129 (pS129; abcam, ab59264), α-synuclein (LB509; abcam, ab27766), tau phosphorylated at Ser 202 and Thr 205 (AT8; ThermoFisher Scientific, MN1020) and amyloid β (6E10; BioLegend, 803004), and polyclonal antibody against tau phosphorylated at Ser 199 and Thr 202 (pS199/202; ThermoFisher Scientific, 44-768G) are commercially available. All experiments with C05-01, C05-03, C05-05, ^{18}F-C05-05, PBB3, ^{11}C-PBB3, PM-PBB3 and ^{18}F- PM-PBB3 were performed under UV-cut light to avoid photo-isomerization of these compounds (Tagai et al., 2020).

Postmortem brain tissues

Postmortem human brains were obtained from autopsies carried out at the Department of Neuroscience of the Mayo Clinic on patients with DLB and MSA, and at the Center for Neurodegenerative Disease Research of the University of Pennsylvania Perelman School of Medicine on patients with AD. Tissues for homogenate binding assays were frozen, and tissues for histochemical, immunohistochemical and autoradiographic labeling were frozen or fixed in 10% neutral buffered formalin followed by embedding in paraffin blocks.

Preparation of recombinant α-synuclein and fibrils

Recombinant mouse and marmoset wild-type α-synuclein and fibrils were prepared as described previously (Masuda-Suzukake et al., 2014; Tarutani et al., 2016; Shimozawa et al., 2017). Briefly, purified α-synuclein (7 -10 mg/ml) was incubated at 37°C in a shaking incubator at 200 rpm in 30 mM Tris-HCl, pH 7.5, containing 0.1% NaN$_3$, for 72 hours. α-synuclein fibrils were pelleted by spinning the assembly mixtures at 113,000 × g for 20 min, resuspended in saline, and sonicated for 3 min (Biomic 7040 Ultrasonic Processor, Seiko). Protein concentrations were determined by high performance liquid chromatography (HPLC) and adjusted to 4 mg/ml by dilution with saline.

Virus preparation

A recombinant adeno associated virus (AAV) was prepared in HEK293T cells by polyethylenimine mediated co-transfection of AAV transfer vector encoding mCherry with rat Synapsin promoter and AAV serotype DJ packaging plasmids, pHelper and pRC-DJ (Cell Biolabs Inc.), as described previously (Nagai et al., 2020). 48 hours after transfection, cells were harvested and lysed in 20 mM HEPES-NaOH, pH 8.0, 150mM NaCl buffer supplemented with 0.5% sodium deoxyholate and 50 units/mL benzonase nuclease (Sigma). AAV particles were next purified with HiTrap heparin column (GE Healthcare) and virus titer was determined by AAVpro® Titration kit (for Real Time PCR) ver2 (TaKaRa).

Stereotaxic surgery

For histochemistry, *ex vivo* examination and *in vivo* longitudinal imaging by two-photon laser scanning, nine-week-old mice anesthetized with 1.5% (v/v) isoflurane were unilaterally injected with 3 μl of recombinant mouse α-synuclein fibrils or 3 μl of saline into striatum (Interaural 3.82 mm, Lateral 2.0 mm, Depth 2.0 mm) via glass capillary. For PET study and *ex vivo* autoradiography, nine-week-old mice anesthetized with 1.5% (v/v) isoflurane were bilaterally injected with 3 μl of recombinant mouse α-synuclein fibrils or 3 μl of saline into striatum. For *in vivo* evaluation of ligands by two-photon laser scanning, mice anesthetized

31

with 1.5% (v/v) isoflurane were unilaterally injected with 3 µl of recombinant mouse α-synuclein fibrils into somatosensory cortex (Interaural 1.98 mm, Lateral 2.5 mm, Depth 0.375 mm). For double inoculation of α-synuclein fibrils and AAV, nine-weeks-old mice anesthetized with 1.5% (v/v) isoflurane were unilaterally injected with 1 µl of purified AAV stock into somatosensory cortex (Interaural 1.98 mm, Lateral 2.5 mm, Depth 0.375 mm) and 3 µl of recombinant mouse α-synuclein fibrils into striatum.

In the marmoset, surgeries were performed under aseptic conditions in fully equipped operating suite. We monitored body temperature, heart rate and SpO$_2$ throughout all surgical procedures. The marmoset (2 years old at the time of surgery) was immobilized by intramuscular injection of ketamine (5-10 mg/kg) and xylazine (0.2-0.5 mg/kg) and intubated by endotracheal tube. Anesthesia was maintained with isoflurane (1-3%, to effect). Prior to surgery, MRI (20 cm bore, Biospec, Avance-III system; Bruker Biospin) and X-ray computed tomography (CT) scans (Accuitomo170, J. MORITA CO.) were performed under anesthesia (isoflurane 1-3%, to effect). Overlay MR and CT images were created using PMOD image analysis software (PMOD Technologies Ltd) to estimate stereotaxic coordinates of target brain structures. For injections, the marmoset underwent surgical procedure to open burr holes (~3 mm diameter) for the injection needle. Recombinant marmoset α-synuclein fibrils (right hemisphere, total 100 µl; 50 µl × 2 regions) and saline (left hemisphere, total 100 µl; 50 µl × 2 regions) were pressure-injected into caudate nucleus (Interaural 9.75 mm) and putamen (Interaural 9.75 mm) by Hamilton syringe mounted into motorized microinjector (UMP3T-2, WPI) held by manipulator (Model 1460, David Kopf, Ltd.) on a stereotaxic frame.

Ex vivo fluorescence examination

Mice were anesthetized with 1.5% (v/v) isoflurane and intraperitoneally administered BF-227 (1.66 mg/kg) and C05-05 (1.66 mg/kg). 2 hours after administration of BF-227 (Kudo et al., 2007) and 90 min after administration of C05-05, mice were then sacrificed by cervical dislocation, and brains were

removed. After quick freezing by powdered dry ice, 20-µm thick frozen sections were prepared by cryostat and mounted in non-fluorescent mounting media (VECTASHIELD; Vector Laboratories). Fluorescence images of brain section with no additional staining were captured by DM4000 microscope (Leica) equipped with custom filter cube (excitation band-pass at 414/23 nm and suppression low-pass with 458 nm cut-off) and BZ-X710 fluorescence microscope (KEYENCE) equipped with Filter set ET-ECFP (Chroma Technology). For immunostaining, sections used for *ex vivo* examination were fixed in 4% paraformaldehyde in phosphate buffered saline (PBS) overnight at 4°C just prior to staining.

Two-photon laser-scanning microscopy

For surgical procedure, animals were anesthetized with a mixture of air, oxygen and isoflurane (3-5% W/V for induction and 2% W/V for surgery) via a facemask, and a cranial window (4.5-5 mm in diameter) was attached over the right somatosensory cortex, centered at 2.5 mm caudal and 2.5 mm lateral from bregma (Holtmaat et al., 2009). Two-photon imaging was performed in awake mice two weeks after cranial window surgery at the earliest. Sulforhodamine 101 dissolved in saline (5 mM) was intraperitoneally administered (4 µl/g body weight) just before initiation of imaging experiments, and 0.05 mg of C05-05, C05-01 and PBB3 dissolved in dimethyl sulfoxide : saline = 1 : 1 (0.05% W/V) was intraperitoneally administered at various time points. Animals were placed on a custom-made apparatus, and real-time imaging was conducted by two-photon laser scanning microscopy (TCS-SP5 MP, Leica) with an excitation wavelength of 850-900 nm. In evaluation of *in vivo* labeling of α-synuclein inclusions with ligands, two-photon imaging was performed before and 5, 30, 60 and 90 min after administration of ligands. In *in vivo* longitudinal imaging of α-synuclein inclusions with C05-05, two-photon imaging was performed 90 min after administration of C05-05. An emission signal was separated by beam splitter (560/10 nm) and simultaneously detected through band-pass filter for ligands (525/50 nm) and sulforhodamine 101 and mCherry (610/75 nm). A single image plane consisted of 1024×1024 pixels, with in-plane pixel size of 0.45 µm. Volume images were

33

acquired up to maximum depth of 200-500 μm from cortical surface with z-step size of 2.5 μm.

Radiosynthesis

[11]C-PE2I, ^{11}C-PBB3, ^{18}F-PM-PBB3 and ^{18}F-C05-01 were radiosynthesized using their desmethyl, tosylate or nitro precursors as described previously (Nagai et al., 2012; Maruyama et al., 2013; Hashimoto et al., 2014; Tagai et al., 2020; Yamasaki et al., 2011). Radiolabeling of ^{18}F-C05-05 was accomplished by ring-opening reaction of (rac)- ^{18}F-epifluorohydrin with a phenolic precursor (C05-03) in the presence of 1.0 N NaOH and dimethylformamide at 130°C for 20 min as described in Figure S5 (Fujinaga et al., 2018). After fluoroalkylation, the crude reaction mixture was transferred into a reservoir for preparative HPLC using Atlantis Prep T3 column (10 × 150 mm, Waters) with a mobile phase consisting of acetonitrile/water (25/75) with 0.1% trifluoroacetic acid (v/v) at a flow rate of 5 ml/min. The fraction corresponding to ^{18}F-C05-05 was collected in a flask containing 100 μl of 25% ascorbic acid solution and Tween 80, and was evaporated to dryness under a vacuum. The residue was dissolved in 3 ml of saline (pH 7.4) to obtain ^{18}F-C05-05. The final formulated product was chemically and radiochemically pure (>95%) as detected by analytical HPLC using Atlantis Prep T3 column (4.6 × 150 mm, Waters) with mobile phase consisting of acetonitrile/water (30/70) with 0.1% trifluoroacetic acid (v/v) at a flow rate of 1 ml/min. Specific activity of ^{18}F-C05-05 at the end of synthesis was 218-260 GBq/μmol, and ^{18}F-C05-05 maintained its radioactive purity exceeding 90% for over 3 hours after formulation.

PET imaging

PET scans were performed by microPET Focus 220 scanner (Siemens Medical Solutions). Mice were anesthetized with 1.5-2.0% isoflurane during all PET procedures. Emission scans were acquired for 90 and 120 min in 3D list mode with an energy window of 350-750 keV immediately after intravenous injection of ^{18}F-C05-01 (23.5 ± 0.2 MBq) and ^{18}F-C05-05 (30.8 ± 0.4 MBq), respectively.

34

Images were reconstructed by either maximum a posteriori methods or filtered back projection by 0.5 mm Hanning filter. All image data were subsequently analyzed using PMOD software (PMOD Technologies). For spatial alignment of PET images, template MRI images generated previously (Maeda et al., 2007) were used in this study. Volumes of interest (VOIs) were manually placed on the striatum, cortex, amygdala and cerebellum. The marmoset was anesthetized with 1-3% isoflurane during all PET procedures. Transmission scans were performed for about 20 min with a Ge-68 source. Emission scans were acquired for 120 min and 90 min in 3D list mode with an energy window of 350-750 keV after intravenous bolus injection of ^{18}F-C05-05 (89.6 ± 15.3 MBq) and ^{11}C-PE2I (89.2 ± 2.0 MBq), respectively. All list-mode data were sorted into 3D sinograms, which were then Fourier-rebinned into 2D sinograms. Images were thereafter reconstructed with filtered back projection using a Hanning filter cut-off at Nyquist frequency (0.5 mm^{-1}). All image data were subsequently analyzed using PMOD software. VOIs were placed on the caudate nucleus, putamen and cerebellum with reference to standard marmoset brain MR image (Hikishima et al., 2011). After anatomical standardization, decay-corrected time-activity curves in each of the VOIs were generated as the regional concentration of radioactivity averaged across the specific time window after radioligand injection. In the striatum and cortex, uptake value ratio to the cerebellum was calculated. To quantify ^{11}C-PE2I binding, BP$_{ND}$ was calculated with a simplified reference tissue model using the cerebellum as a reference region, and the caudate nucleus and the putamen as signal-rich regions.

Histological examination

Mice were deeply anesthetized and sacrificed by saline perfusion, and brains were subsequently dissected and fixed in 4% paraformaldehyde in PBS overnight at 4°C. After cryo-protection in PBS containing 20% sucrose, brains were embedded and frozen in OCT compound (SaKuRa), and 20-μm thick fixed frozen sections were prepared by cryostat. The marmoset was deeply anesthetized with an overdose of sodium pentobarbital (80 mg/kg, intravenous administration) and

transcardially perfused with saline at 4°C, followed by 4% paraformaldehyde in PBS, pH 7.4. The brain was removed from the skull, postfixed in the same fresh fixative overnight, saturated with 30% sucrose in phosphate buffer at 4°C, and then cut serially into 40-μm-thick sections on a freezing microtome. For fluorescence labeling with ligands, mouse fixed frozen sections, marmoset fixed sections, 6-μm thick deparaffinized postmortem human brain sections and 20-μm thick fresh frozen human brain sections post-fixed in 4% paraformaldehyde in PBS were incubated in 20% and 50% ethanol containing 30 μM ligand, respectively, at room temperature for 30 min. The samples were rinsed with 20% or 50% ethanol for 5 min, dipped into distilled water twice for 3 min each, and mounted in VECTASHIELD. Fluorescence images were captured by a DM4000 microscope equipped with a custom filter cube and a BZ-X710 fluorescence microscope equipped with Filter set ET-ECFP. Sections labeled with ligands in fluorescence microscopy, *ex vivo* examination and autoradiography and their adjacent sections were immunostained with pS129, LB509, pS199/202 and AT8 antibodies with antigen retrieval by autoclaving, and with 6E10 antibodies with antigen retrieval by formic acid. Immunolabeling was then examined using DM4000 and BZ-X710. Images were analyzed using ImageJ software (NIH Image).

Autoradiography

In vitro autoradiography was performed using 6-μm-thick deparaffinized sections derived from MSA brains, 20-μm-thick fresh frozen sections post-fixed in 4% paraformaldehyde in PBS derived from DLB brains and 40-μm-thick fixed sections derived from α-Syn marmoset. For labeling with ^{18}F-C05-05, sections were pre-incubated in 50 mM Tris-HCl buffer, pH 7.4, containing 20% ethanol at room temperature for 30 min, and incubated in 50 mM Tris-HCl buffer, pH 7.4, containing 20% ethanol and ^{18}F-C05-05 (10 nM; specific radioactivity: 260 GBq/μmol) at room temperature for 60 min. Excess concentration (10 μM) of C05-05 was added to the reaction to determine nonspecific radioligand binding. The samples were then rinsed with ice-cold Tris-HCl buffer containing 20% ethanol

36

twice for 2 min, and dipped into ice-cold water for 10 sec. The sections labeled with ^{18}F-C05-05 were subsequently dried with warm air, and exposed to an imaging plate (BAS-MS2025; Fuji Film). *Ex vivo* autoradiography was performed in mice used in PET imaging. Mice were anesthetized with 1.5% (v/v) isoflurane and intravenously administrated ^{18}F-C05-05 (27.8 ± 0.2 MBq, specific radioactivity: 63 GBq/μmol). 90 min after administration of ^{18}F-C05-05, mice were then sacrificed by cervical dislocation, and the brains were removed. After quick freezing with powdered dry ice, 20-μm thick frozen sections were prepared by cryostat and exposed to an imaging plate. The imaging plate was scanned by BAS-5000 system (Fuji Film) to acquire autoradiograms. Images were analyzed using Multi Gauge software (Fuji Film).

In vitro binding assay

Frozen tissues derived from the amygdala of a DLB patient and the frontal cortex of an AD patient were homogenized in 50 mM Tris-HCl buffer, pH 7.4, containing protease inhibitor cocktail (cOmplete^{TM}, EDTA-free; Roche), and stored at -80°C until analyses. To assay radioligand binding with homologous blockade, these homogenates (100 μg tissue) were incubated with 5 nM ^{18}F-C05-05 (specific radioactivity: 63 GBq/μmol), 5 nM ^{11}C-PBB3 (specific radioactivity: 93.4 ± 24 GBq/μmol) or 1 nM ^{18}F-PM-PBB3 (specific radioactivity: 183.3 ± 89.2 GBq/μmol) in the absence or presence of non-radiolabeled C05-05, PBB3 or PM-PBB3 at varying concentrations ranging from $1{\times}10^{-11}$ to $5{\times}10^{-7}$ M in Tris-HCl buffer containing 10% ethanol, pH 7.4, for 30 min at room temperature. Non-specific binding of ^{18}F-C05-05, ^{11}C-PBB3 and ^{18}F-PM-PBB3 was determined in the presence of $5{\times}10^{-7}$ M C05-05, PBB3 and PM-PBB3, respectively. Samples were run in triplicate. Concentration of the competitor inducing 50% inhibition (IC50) was determined by using non-linear regression to fit a concentration-binding plot to one-site and two-site binding models derived from the Cheng-Prusoff equation with GraphPad Prism version 5.0 (GraphPad Software), followed by F-test for model selection.

QUANTIFICATION AND STATISTICAL ANALYSIS

Statistical significance of the data was analyzed with GraphPad Prism version 5.0. For comparison of multiple groups, data were analyzed by one-way ANOVA with post-hoc Tukey's HSD test. For comparison of multiple groups and regions, data were analyzed by two-way repeated-measures ANOVA with Bonferroni's post hoc analysis.

DATA AND SOFTWARE AVAILABILITY

Requests for data that support the finding of this study should be directed to the Lead Contact, Maiko Ono (ono.maiko@qst.go.jp) and will be available upon reasonable request.

SUPPLEMENTAL INFORMATION

Table S1. Antemortem clinical diagnosis and neuropathologic description of postmortem human brain tissues, Related to Figure 1, 7.

Figure S1. Immunostaining of DLB and AD brain sections used for characterization of ligands, Related to Figure 1.

Figure S2. Temporal changes in the distribution of phosphorylated α-synuclein inclusions in mice injected with α-synuclein fibrils into the striatum, Related to Figure 3-5.

Figure S3. *Ex vivo* examination of brain sections from a mouse injected with α-synuclein fibrils into the neocortex, Related to Figure 2.

Figure S4. *Ex vivo* examination of brain sections from control mice, Related to Figure 3.

Figure S5. Radiosynthesis of ^{18}F-C05-05, Related to Figure 5-7.

Figure S6. Brain uptake of ^{18}F-C05-01 in wild-type mice, Related to Figure 5.

Figure S7. Time-radioactivity curves of ^{18}F-C05-05 in the amygdala of α-Syn and control mice, Related to Figure 5.

Figure S8. Time-radioactivity curves of ^{18}F-C05-05 in the brain of an α-Syn marmoset, Related to Figure 6.

REFERENCES

C.H. Adler, T.G. Beach, J.G. Hentz, H.A. Shill, J.N. Caviness, E. Driver-Dunckley, M.N. Sabbagh, L.I. Sue, S.A. Jacobson, C.M. Belden, B.N. Dugger, Low clinical diagnostic accuracy of early vs advanced Parkinson disease: clinicopathologic study. *Neurology* **83**, 406-412 (2014). doi:10.1212/WNL.0000000000000641

K. Ando, S. Obayashi, Y. Nagai, A. Oh-Nishi, T. Minamimoto, M. Highchi, T. Inoue, T. Itoh, T. Suhara, PET analysis of dopaminergic neurodegeneration in relation to immobility in the MPTP-treated common marmoset, a model for Parkinson's disease. *PLoS One* **7**, e46371 (2012). doi:10.1371/journal.pone.0046371

M. Baba, S. Nakajo, P.H. Tu, T. Tomita, K. Nakaya, V.M. Lee, J.Q. Trojanowski, T. Iwatsubo, Aggregation of alpha-synuclein in Lewy bodies of sporadic Parkinson's disease and dementia with Lewy bodies. *Am. J. Pathol.* **152**, 879-884 (1998).

T.J. Betthauser, K.A. Cody, M.D. Zammit, D. Murali, A.K. Converse, T.E. Barnhart, C.K. Stone, H.A. Rowley, S.C. Johnson, B.T. Christian, In Vivo Characterization and Quantification of Neurofibrillary Tau PET Radioligand ^{18}F-MK-6240 in Humans from Alzheimer Disease Dementia to Young Controls. *J. Nucl. Med.* **60**, 93-99 (2019). doi:10.2967/jnumed.118.209650

H. Braak, K. Del Tredici, U. Rüb, R.A. de Vos, E.N. Jansen Steur, E. Braak, Staging of brain pathology related to sporadic Parkinson's disease. *Neurobiol. Aging* **24**, 197-211 (2003).

P. Brundin, K.D. Dave, J.H. Kordower, Therapeutic approaches to target alpha-synuclein pathology. *Exp. Neurol.* **298**, 225-235 (2017). doi:10.1016/j.expneurol.2017.10.003

D.T. Chien, A.K. Szardenings, S. Bahri, J.C. Walsh, F. Mu, C. Xia, W.R. Shankle, A.J. Lerner, M.Y. Su, A. Elizarov, H.C. Kolb, Early clinical PET imaging results with the novel PHF-tau radioligand [F-18]-T808. *J. Alzheimers Dis.* **38**, 171-184 (2014). doi:10.3233/JAD-130098

B.K. Choi, M.G. Choi, J.Y. Kim, Y. Yang, Y. Lai, D.H. Kweon, N.K. Lee, Y.K. Shin, Large α-synuclein oligomers inhibit neuronal SNARE-mediated vesicle docking. *Proc. Natl. Acad. Sci. U. S. A.* **110**, 4087-4092 (2013). doi:10.1073/pnas.1218424110

V. Deramecourt, S. Bombois, C.A. Maurage, A. Ghestem, H. Drobecq, E. Vanmechelen, F. Lebert, F. Pasquier, A. Delacourte, Biochemical staging of synucleinopathy and amyloid deposition in dementia with Lewy bodies. *J. Neuropathol. Exp. Neurol.* **65**, 278-288 (2006).

P. Desplats, H.-J. Lee, E.-J. Bae, C. Patrick, E. Rockenstein, L. Crews, B. Spencer, E. Masliah, S.-J. Lee, Inclusion formation and neuronal cell death through neuron-to-neuron transmission of alpha-synuclein. *Proc. Natl. Aced. Sci. U.S.A.* **106**, 13010-13015 (2009). doi:10.1073/pnas.0903691106

D.W. Dickson, W. Lin, W.K. Liu, S.H. Yen, Multiple system atrophy: a sporadic synucleinopathy. *Brain Pathol.* **9**, 721-732 (1999).

A.W.P. Fitzpatrick, B. Falcon, S. He, A.G. Murzin, G. Murshudov, H.J. Garringer, R.A. Crowther, B. Ghetti, M. Goedert, S.H.W. Scheres, Cryo-EM structures of tau filaments from Alzheimer's disease. *Nature* **547**, 185-190 (2017). doi:10.1038/nature23002

B. Falcon, W. Zhang, A.G. Murzin, G. Murshudov, H.J. Garringer, R. Vidal, R.A. Croether, B. Ghetti, S.H.W. Scheres, M. Goedert, Structures of filaments from Pick's disease reveal a novel tau protein fold. *Nature* **561**, 137-140 (2018). doi:10.1038/s41586-018-0454-y

M. Fujinaga, T. Ohkubo, T. Yamasaki, Y. Zhang, W. Mori, M. Hanyu, K. Kumata, A. Hatori, L. Xie, N. Nengaki, M.R. Zhang, Automated Synthesis of (rac)-, (R)-, and (S)-[18F]Epifluorohydrin and Their Application for Developing PET Radiotracers Containing a 3-[18F]Fluoro-2-hydroxypropyl Moiety. *ChemMedChem* **13**, 1723-1731 (2018). doi:10.1002/cmdc.201800359

R. Gordon, E.A. Albornoz, D.C. Christie, M.R. Langley, V. Kumar, S. Mantovani, A.A.B. Robertson, M.S. Butler, D.B. Rowe, L.A. O'Neill, A.G. Kanthasamy, K. Schroder, M.A. Cooper, T.M. Woodruff, Inflammasome inhibition prevents α-synuclein pathology and dopaminergic neurodegeneration in mice. *Sci. Transl. Med.* **10**, eaah4066 (2018). doi:10.1126/scitranslmed.aah4066

R. Guerrero-Ferreira, N.M. Taylor, A.A. Arteni, P. Kumari, D. Mona, P. Ringler, M. Britschgi, M.E. Lauer, A. Makky, J. Verasdonck, R. Riek, R. Melki, B.H. Meier, A. Böckmann, L. Bousset, H. Stahlberg, Two new polymorphic structures of human full-length alpha-synuclein fibrils solved by cryo-electron microscopy. *Elife* **8**, (2019). doi:10.7554/eLife.48907

R. Guerrero-Ferreira, N.M. Taylor, D. Mona, P. Ringler, M.E. Lauer, R. Riek, M. Britschgi, H. Stahlberg, Cryo-EM structure of alpha-synuclein fibrils. *Elife* **7**, (2018). doi:10.7554/eLife.36402

M. Goedert, Alpha-synuclein and neurodegenerative diseases. *Nat. Rev. Neurosci.* **2**, 492-501 (2001).

M. Goedert, Y. Yamaguchi, S.K. Mishra, M. Highchi, N. Sahara, Tau Filaments and the Development of Positron Emission Tomography Tracers. *Front. Neurol.* **9**, 70 (2018). doi:10.3389/fneur.2018.00070

R. Harada, A. Ishiki, H. Kai, N. Sato, K. Furukawa, S. Furumoto, T. Tago, N. Tomita, S. Watanuki, K. Hiraoka, Y. Ishikawa, Y. Funaki, T. Nakamura, T. Yoshikawa, R. Iwata, M. Tashiro, H. Sasano, T. Kitamoto, K. Yanai, H. Arai, Y. Kudo, N. Okamura, Correlations of ^{18}F-THK5351 PET with post-mortem burden of tau and astrogliosis in Alzheimer's disease. *J. Nucl. Med.* **59**, 671-674 (2017). doi:10.2967/jnumed.117.197426

H. Hashimoto, K. Kawamura, N. Igarashi, M. Takei, T. Fujishiro, Y. Aihara, S. Shiomi, M Muto, T. Ito, K. Furutsuka, T Yamasaki, J. Yui, L. Xie, M. Ono, A. Hatori, K Nemoto, T Suhara, M. Higuchi, M. R. Zhang, Radiosynthesis, photoisomerization, biodistribution, and metabolite analysis of ^{11}C-PBB3 as a clinically useful PET probe for imaging of tau pathology. *J. Nucl. Med*. **55**, 1532-1538 (2014).

M.X. Henderson, J.Q. Trojanowski, V.M. Lee, α-synuclein pathology in Parkinson's disease and related α-synucleinopathies. *Neurosci. Lett.* **709**, 134316 (2019). doi:10.1016/j.neulet.2019.134316

K. Hikishima, M.M. Quallo, Y Komaki, M Yamada, K Kawai, S Momoshima, H.J. Okano, E Sasaki, N Tamaoki, R.N. Lemon, A. Iriki, H. Okano, Population-averaged standard template brain atlas for the common marmoset (Callithrix jacchus). *Neuroimage* **54**, 2741–2749 (2011).

A. Holtmaat, T. Bonhoeffer, D.K. Chow, J. Chuckowree, V. De Paola, S.B. Hofer, M. Hübener, T. Keck, G. Knott, W.-C.A. Lee, R. Mostany, T.D. Mrsic-Flogel, E. Nedivi, C. Portera-Cailliau, K. Svoboda, J.T. Trachtenberg, L. Wilbrecht, Long-term, high-resolution imaging in the mouse neocortex through a chronic cranial window. *Nat. Protoc.* **4**, 1128-1144 (2009). doi:10.1038/nprot.2009.89

R.B. Innis, J.P. Seibyl, B.E. Scanley, M. Laruelle, A. Abi-Dargham, E. Wallace, R.M. Baldwin, Y. Zea-Ponce, S. Zoghbi, S. Wang, Single photon emission computed tomographic imaging demonstrates loss of striatal dopamine transporters in Parkinson disease. *Proc. Natl. Aced. Sci. U.S.A.* **90**, 11965-11969 (1993).

D.J. Irwin, M. Grossman, D. Weintraub, H.I. Hurtig, J.E. Duda, S.X. Xie, E.B. Lee, V.M. Van Deerlin, O.L. Lopez, J.K. Kofler, P.T. Nelson, G.A. Jicha, R. Woltjer, J.F. Quinn, J. Kaya, J.B. Leverenz, D. Tsuang, K. Longfellow, D. Yearout, W. Kukull, C.D. Keene, T.J. Montine, C.P. Zabetian, J.Q. Trojanowski, Neuropathological and genetic correlates of survival and dementia onset in synucleinopathies: a retrospective analysis. *Lancet Neurol.* **16**, 55-65 (2017). doi:10.1016/S1474-4422(16)30291-5

J. Joutsa, M. Gardberg, M. Röyttä, V. Kaasinen, Diagnostic accuracy of parkinsonism syndromes by general neurologists. *Parkinsonism Relat. Disord.* **20**, 840-844 (2014). doi:10.1016/j.parkreldis.2014.04.019

A. Kikuchi, A. Takeda, N. Okamura, M. Tashiro, T. Hasegawa, S. Furumoto, M.

44

Kobayashi, N. Sugeno, T. Baba, Y. Miki, F. Mori, K. Wakabayashi, Y. Funaki, R. Iwata, S. Takahashi, H. Fukuda, H. Arai, Y. Kudo, K. Yanai, Y. Itoyama, In vivo visualization of alpha-synuclein deposition by carbon-11-labelled 2-[2-(2-dimethylaminothiazol-5-yl)ethenyl]-6-[2-(fluoro)ethoxy]benzoxacole positron emission tomography in multiple system atrophy. *Brain* **133**, 1772-1778 (2010). doi:10.1093/brain/awq091

C. Kim, D.-H. Ho, J.-E. Suk, S. You, S. Michael, J. Kang, S.J. Lee, E. Masliah, D. Hwang, H.-J. Lee, S.-J. Lee, Neuron-released oligomeric α-synuclein is an endogenous agonist of TLR2 for paracrine activation of microglia. *Nat. Commun.* **4**, 1562 (2013). doi:10.1038/ncomms2534

W.E. Klunk, H. Engler, A. Nordberg, Y. Wang, G. Blomqvist, D.P. Holt, M. Bergström, I. Savitcheva, G.F. Huang, S. Estrada, B. Ausén, M.L. Debnath, J. Barletta, J.C. Price, J. Sandell, B.J. Lopresti, A. Wall, P. Koivisto, G. Mathis, B. Långström, Imaging brain amyloid in Alzheimer's disease with Pittsburgh Compound-B. *Ann. Neurol.* **55**, 306-319 (2004).

S. Koga, M. Ono, N. Sahara, M. Higuchi, D.W. Dickson, Fluorescence and autoradiographic evaluation of tau PET ligand PBB3 to α-synuclein pathology. *Mov. Disord.* **32**, 884-892 (2017). doi:10.1002/mds.27013

Y. Kudo, N. Okamura, S. Furumoto, M. Tashiro, K. Furukawa, M. Maruyama, M. Ito, R. Iwata, K. Yanai, H. Arai, 2-(2-[2-Dimethylaminothiazol-5-yl]ethenyl)-6- (2-[fluoro]ethoxy)benzoxazole: a novel PET agent for in vivo detection of dense amyloid plaques in Alzheimer's disease patients. *J. Nucl. Med.* **48**, 553-561 (2007).

L. Lemoine, A. Leuzy, K. Chiotis, E. Rodriguez-Vieitez, A. Nordberg, Tau positron emission tomography imaging in tauopathies: The added hurdle of off-target binding. *Alzheimers Dement. (Amst)* **10**, 232-236 (2018).

doi:10.1016/j.dadm.2018.01.007

B. Li, P. Ge, K.A. Murray, P. Sheth, M. Zhang, G. Nair, M.R. Sawaya, W.S. Shin, D.R. Boyer, S. Ye, D.S. Eisenberg, Z.H. Zhou, L. Jiang, Cryo-EM of full-length α-synuclein reveals fibril polymorpha with a common structural kernel. *Nat. Commun.* **9**, 3609 (2018). doi:10.1038/s41467-018-05971-2

Y. Li, C. Zhao, F. Luo, Z. Liu, X. Gui, Z. Luo, X. Zhang, D. Li, C. Liu, X. Li, Amyloid fibtil structure of α-synuclein determined by cryo-electron microscopy. *Cell Res.* **28**, 897-903 (2018). Doi:10.1038/s41422-018-0075-x

K.C. Luk, V. Kehm, J. Carroll, B. Zhang, P. O'Brien, J.Q. Trojanowski, V.M. Lee, Pathological α-synuclein transmission initiates Parkinson-like neurodegeneration in nontransgenic mice. *Science* **338**, 949-953 (2012a). doi:10.1126/science.1227157

K.C. Luk, V. Kehm, J. B. Zhang, P. O'Brien, J.Q. Trojanowski, V.M. Lee, Intracerebral inoculation of pathological α-synuclein initiates a rapidly progressive neurodegenerative α-synucleinopathy in mice. *J. Exp. Med.* **209**, 975-986 (2012b). doi:10.1084/jem.20112457

J. Maeda, B. Ji, T. Irie, T. Tomiyama, M. Maruyama, T. Okauchi, M. Staufenbiel, N. Iwata, M Ono, T. C. Saido, K. Suzuki, H. Mori, M. Higuchi, T. Suhara, Longitudinal, quantitative assessment of amyloid, neuroinflammation, and nati-amyloid treatment in a living mouse model of Alzheimer's disease enabled by positron emission tomography. *J. Neurosci.* **27**, 10957-10968 (2007).

M. Maruyama, H. Shimada, T. Suhara, H. Shinotoh, B. Ji, J. Maeda, M.R. Zhang, J.Q. Trojanowski, V.M. Lee, M. Ono, K. Masamoto, H. Takano, N. Sahara, N. Iwata, N. Okamura, S. Furumoto, Y. Kudo, Q. Chang, T. C. Saido, A. Takashima, J. Lewis, M. K. Jang, I. Aoki, H. Ito, M. Higuchi, Imaging of tau pathology in a

46

tauopathy mouse model and in Alzheimer patients compared to normal controls. *Neuron* **79**, 1094-1108 (2013). doi:10.1016/j.neuron.2013.07.037

M. Masuda-Suzukake, T. Nonaka, M. Hosokawa, M. Kubo, A. Shimozawa, H. Akiyama, M. Hasegawa, Pathological alpha-synuclein propagates through neural networks. *Acta Neuropathol. Commun.* **2**, 88 (2014). doi:10.1186/s40478-014-0088-8

M. Masuda-Suzukake, T. Nonaka, M. Hosokawa, T. Oikawa, T. Arai, H. Akiyama, D.M. Mann, M. Hasegawa, Prion-like spreading of pathological α-synuclein in brain. *Brain* **136**, 1128-1138 (2013). doi:10.1093/brain/awt037

P. Miranda-Azpiazu, M. Svedberg, M. Higuchi, M. Ono, Z. Jia, D. Sunnemark, C.S. Elmore, M. Schou, A. Varrone, Identification and *in vitro* characterization of C05-01, a PBB3 derivative with improved affinity for alpha-synuclein. *Brain Res.* **1749**, 147131 (2020). doi:10.1016/j.brainres.2020.147131

A. Mueller, S. Bullich, O. Barret, J. Madonia, M. Berndt, C. Papin, A. Perrotin, N. Koglin, H. Kroth, A. Pfeifer, G. Tamagnan, J.P. Seibyl, K. Marek, S. de Santi, L.M. Dinkelborg, A.W. Stephens, Tau PET imaging with ^{18}F-PI-2620 in patients with Alzheimer's disease and healthy controls: a first-in-human study. *J. Nucl. Med.* (2019). doi:10.2967/jnumed.119.236224

Y. Nagai, T. Minamimoto, K. Ando, S. Obayashi, H. Ito, N. Ito, T. Suhara, Correlation between decreased motor activity and dopaminergic degeneration in the ventrolateral putamen in monkeys receiving repeated MPTP administrations: a positron emission tomograohy study. *Neurosci. Res.* **73**, 61-67 (2012). doi:10.1016/j.neures.2012.02.007

Y. Nagai, N. Miyakawa, H. Takuwa, Y. Hori, K. Oyama, B. Ji, M. Takahashi, X. P. Huang, S. T. Slocum, J. F. DiBerto, Y. Xiong, T. Urushihata, T. Hirabayashi, A

Fujimoto, K. Mimura, J. G. English, J. Liu, K. Inoue, K. Kumata, C. Seki, M. Ono, M. Shimojo, M. R. Zhang, Y. Tomita, T. Suhara, M. Takada, M. Higuchi, J. Jin, B. L. Roth, T. Minaminoto, Deschloroclozapine: a potent and selective chemogenetic actuator enables rapid neuronal and behavioral modulations in mice and monkeys. *Nat. Neurosci.* (2020). doi: 10.1038/s41593-020-0661-3

V.M. Nemani, W. Lu, V. Berge, K. Nakamura, B. Onoa, M.K. Lee, F.A. Chaudhry, R.A. Nicoll, R.H. Edwards, Increased expression of alpha-synuclein reduces neurotransmitter release by inhibiting synaptic vesicle reclustering after endocytosis. *Neuron* **65**, 66-79 (2010). doi:10.1016/j.neuron.2009.12.023

K. P. Ng, T. A. Pascoal, S. Mathotaarachchi, J. Therriault, M. S. Kang, M. Shin, M. C. Guiot, Q. Guo, R. Harada, R. A. Comley, G. Massarweh, J. P. Soucy, N. Okamura, S. Gauthier, P. Rosa-Neto, Monoamine oxidase B inhibitor, selegiline, reduces ^{18}F-THK5351 uptake in the human brain. *Alzheimers Res. Ther.* **9**, 25 (2017). doi:10.1186/s13195-017-0253-y

R. Ni, B. Ji, M. Ono, N. Sahara, M. R. Zhang, I. Aoki, A. Nordberg, T. Suhara, M. Higuchi, Comparative In Vitro and In Vivo Quantifications of Pathologic Tau Deposits and Their Association with Neurodegeneration in Tauopathy Mouse Models. *J. Nucl. Med.* **59**, 960-966 (2018). doi:10.2967/jnumed.117.201632

M. Ono, N. Sahara, K. Kumata, B. Ji, R. Ni, S. Koga, D. W. Dickson, J. Q. Trojanowski, V. M. Lee, M. Yoshida, I. Hozumi, Y. Yoshiyama, J. C. van Swieten, A. Nordberg, T. Suhara, M. R. Zhang, M. Higuchi, Distinct binding of PET ligands PBB3 and AV-1451 to tau fibril strains in neurodegenerative tauopathies. *Brain* **140**, 764-780 (2017). doi:10.1093/brain/aww339

D.G. Ordonez, M.K. Lee, M.B. Feany, α-synuclein induces mitochondrial dysfunction through spectrin and the actin cytoskeleton. *Neuron* **97**, 108-124 (2018). doi:10.1016/j.neuron.2017.11.036

48

A. Perez-Soriano, J.E. Arena, K. Dinelle, Q. Miao, J. McKenzie, N. Neilson, A. Puschmann, P. Schaffer, H. Shinotoh, J. Smith-Forrester, E. Shahinfard, N. Vafai, D. Wile, Z. Wszolek, M. Higuchi, V. Sossi, A.J. Stoessl, PBB3 imaging in Parkinsonian disorders: Evidence for binding to tau and other proteins. *Mov. Disord.* **32**, 1016-1024 (2017). doi:10.1002/mds.27029

Y. Saito, A. Kawashima, N.N. Ruberu, H. Fujiwara, S. Koyama, M. Sawabe, T. Arai, H. Nagura, H. Yamanouchi, M. Hasegawa, T. Iwatsubo, S. Murayama, Accumulation of phosphorylated alpha-synuclein in aging human brain. *J. Neuropathol. Exp. Neurol.* **62**, 644-654 (2003).

S. Sanabria Bohórquez, J. Marik, A. Ogasawara, J.N. Tinianow, H.S. Gill, O. Barret, G. Tamagnan, D. Alagille, G. Ayalon, P. Manser, T. Bengtsson, M. Ward, S.P. Willians, G.A. Kerchner, J.P. Seibyl, K. Marek, R.M. Weimer, [^{18}F]GTP1 (Genentech Tau Probe 1), a radioligand for detecting neurofibrillary tangle tau pathology in Alzheimer's disease. *Eur. J. Nucl. Med. Mol. Imaging* **46**, 2077-2089 (2019). doi:10.1007/s00259-019-04399-0

C. Scherfler, J. Schwarz, A. Antonini, D. Grosset, F. Valldeoriola, K. Marek, W. Oertel, E. Tolosa, A.J. Lees, W. Poewe, Role of DAT-SPECT in the diagnostic work up of Parkinsonism. *Mov. Disord.* **22**, 1229-1238 (2007).

M. Schweighauser, Y. Shi, A. Tarutani, F. Kametani, A.G. Murzin, B. Ghetti, T. Matsubara, T. Tomita, T. Ando, K. Hasegawa, S. Murayama, M. Yoshida, M. Hasegawa, S.H.W. Scheres, M. Goedert, Structures of α-Synuclein filaments from multiple system atrophy. *Nature* (2020). doi:10.1038/s41586-020-2317-6

D. Scott, S. Roy, α-Synuclein inhibits intersynaptic vesicle mobility and maintains recycling-pool homeostasis. *J. Neurosci.* **32**, 10129-10135 (2012)

L.C. Serpell, J. Berriman, R. Jakes, M. Goedert, R.A. Crowther, Fiber diffraction of synthetic alpha-synuclein filaments shows amyloid-like cross-beta conformation. *Proc. Natl. Acad. Sci. U. S. A.* **97**, 4897-4902 (2000)

A. Shimozawa, M. Ono, D. Takahara, A. Tarutani, S. Imura, M. Masuda-Suzukake, M. Higuchi, K Yanai, S Hisanaga, M Hasegawa, Propagation of pathological α-synuclein in marmoset brain. *Acta Neuropathol. Commun.* **5**, 12 (2017). doi:10.1186/s40478-017-0413-0

M.G. Spillantini, R.A. Crowther, R. Jakes, N.J. Cairns, P.L. Lantos, M. Goedert, Filamentous alpha-synuclein inclusions link multiple system atrophy with Parkinson's disease and dementia with Lewy bodies. *Neurosci. Lett.* **251**, 205-208 (1998a)

M.G. Spillantini, R.A. Crowther, R. Jakes, M. Hasegawa, M. Goedert, alpha-Synuclein in filamentous inclusions of Lewy bodies from Parkinson's disease and dementia with lewy bodies. *Proc. Natl. Acad. Sci. U. S. A.* **95**, 6469-6473 (1998b)

K. Tagai, M. Ono, M. Kubota, S. Kitamura, K. Takahata, C. Seki, Y. Takado, H. Shinotoh, Y. Sano, Y. Yamamoto, K. Matsuoka, H. Takuwa, M. Shimojo, M. Takahashi, K. Kawamura, T. Kikuchi, M. Okada, H. Akiyama, H. Suzuki, M. Onaya, T. Takeda, K. Arai, N. Arai, N. Araki, Y. Saito, J. Q. Trojanowski, V. M.-Y. Lee, S. K. Mishra, Y. Yamaguchi, Y. Kimura, M. Ichise, Y. Tomita, M.-R. Zhang, T. Suhara, M. Shigeta, N. Sahara, M. Higuchi, H. Shimada, High-contrast in vivo imaging of tau pathologies in Alzheimer's and non-Alzheimer's disease tauopathies. *Neuron* (2020). in press

A. Tarutani, G. Suzuki, A. Shimozawa, T. Nonaka, H. Akiyama, S. Hisanaga, M. Hasegawa, The effect of fragmented pathogenic alpha-synuclein seeds on prion-like propagation. *J. Biol. Chem.* **291**, 18675-18688 (2016). doi:10.1074/jbc.M116.734707

M. Verdurand, E. Levigoureux, S. Lancelot, W. Zeinyeh, T. Billard, I. Quadrio, A. Perret-Liaudet, L. Zimmer, F. Chauveau, Amyloid-Beta Radiotracer [^{18}F]BF-227 Does Not Bind to Cyroplasmic Gkial Inclusions of Postmortem Multiple System Atrophy Brain Tissue. *Contrast Mol. Imaging* (2018). doi:10.1155/2018/9165458

C. Vermeiren, P. Motte, D. Viot, G. Mairet-Coello, J. P. Courade, M. Citron, J. Mercier, J. Hannestad, M. Gillard, The tau positron-emission tomography tracer AV-1451 binds with similar affinities to tau fibrils and monoamine oxidases. *Mov. Disord.* **33**, 273-281 (2017). doi:10.1002/mds.27271

K. Wakabayashi, S. Hayashi, A. Kakita, M. Yamada, Y. Toyoshima, M. Yoshimoto, H. Takahashi, Accumulation of alpha-synuclein/NACP is a cytopathological feature common to Lewy body disease and multiple system atrophy. *Acta Neuropathol.* **96**, 445-452 (1998a).

K. Wakabayashi, M. Yoshimoto, S. Tsuji, H. Takahashi, Alpha-synuclein immunoreactivity in glial cytoplasmic inclusions in multiple system atrophy. *Neurosci. Lett.* **49**, 180-182 (1998b).

L. Wang, U. Das, D.A. Scott, Y. Tang, P.J. McLean, S. Roy, α-synuclein multimers cluster synaptic vesicles and attenuate recycling. *Curr. Biol.* **24**, 2319-2326 (2014). doi:10.1016/j.cub.2014.08.027

D.F. Wong, R.A. Comley, H. Kuwabara, P.B. Rosenberg, S.M. Resnick, S. Ostrowitzki, C. Vozzi, F. Boess, E. Oh, C.G. Lyketsos, M. Honer, L. Gobbi, G. Klein, N. George, L. Gapasin, K. Kitzmiller, J. Roberts, J. Sevigny, A. Nandi, J. Brasic, C. Mishra, M. Thambisetty, A. Mogekar, A. Mathur, M. Albert, R.F. Dannals, E. Borroni, Characterization of 3 Novel Tau Radiopharmaceuticals, ^{11}C-RO-963, ^{11}C-RO-643, and ^{18}F-RO-948, in Healthy Controls and in Alzheimer Subjects. *J. Nucl. Med.* **59**, 1869-1876 (2018). doi:10.2967/jnumed.118.209916

Y.C. Wong, D. Krainc, α-synuclein toxicity in neurodegeneration: mechanism and therapeutic strategies. *Nat. Med.* **23**, 1-13 (2017). doi:10.1038/nm.4269

T. Yamasaki, M. Fujinaga, Y. Yoshida, K. Kumata, J. Yui, K. Kawamura, A. Hatori, T. Fukumura, M.R. Zhang, Radiosynthesis and preliminary evaluation of 4-[^{18}F]fluoro-N-[4-[6-(isopropylamino)pyrimidin-4-yl]-1,3-thiazol-2-yl]-N-methylbenzamide as a new positron emission tomography ligand for metabotropic glutamate receptor subtype 1. *Bioorg. Med. Chem. Lett.* **21**, 2998-3001 (2011). doi: 10.1016/j.bmcl.2011.03.046

M.-L. Yang, L. Hasadsri, W.S. Woods, J.M. George, Dynamic transport and localization of alpha-synuclein in primary hippocampal neurons. *Mol. Neurodegener.* **5**, 9 (2010). doi:10.1186/1750-1326-5-9

W. Zhang, A. Tarutani, K.L. Newell, A.G. Murzin, T. Matsubara, B. Falcon, R. Vidal, H.J. Garringer, Y. Shi, T. Ikeuchi, S. Murayama, B. Ghetti, M. Hasegawa, M. Goedert, S.H.W. Scheres, Novel tau filament fold in corticobasal degeneration. *Nature* **580**, 283-287 (2020). doi:10.1038/s41586-020-2043-0
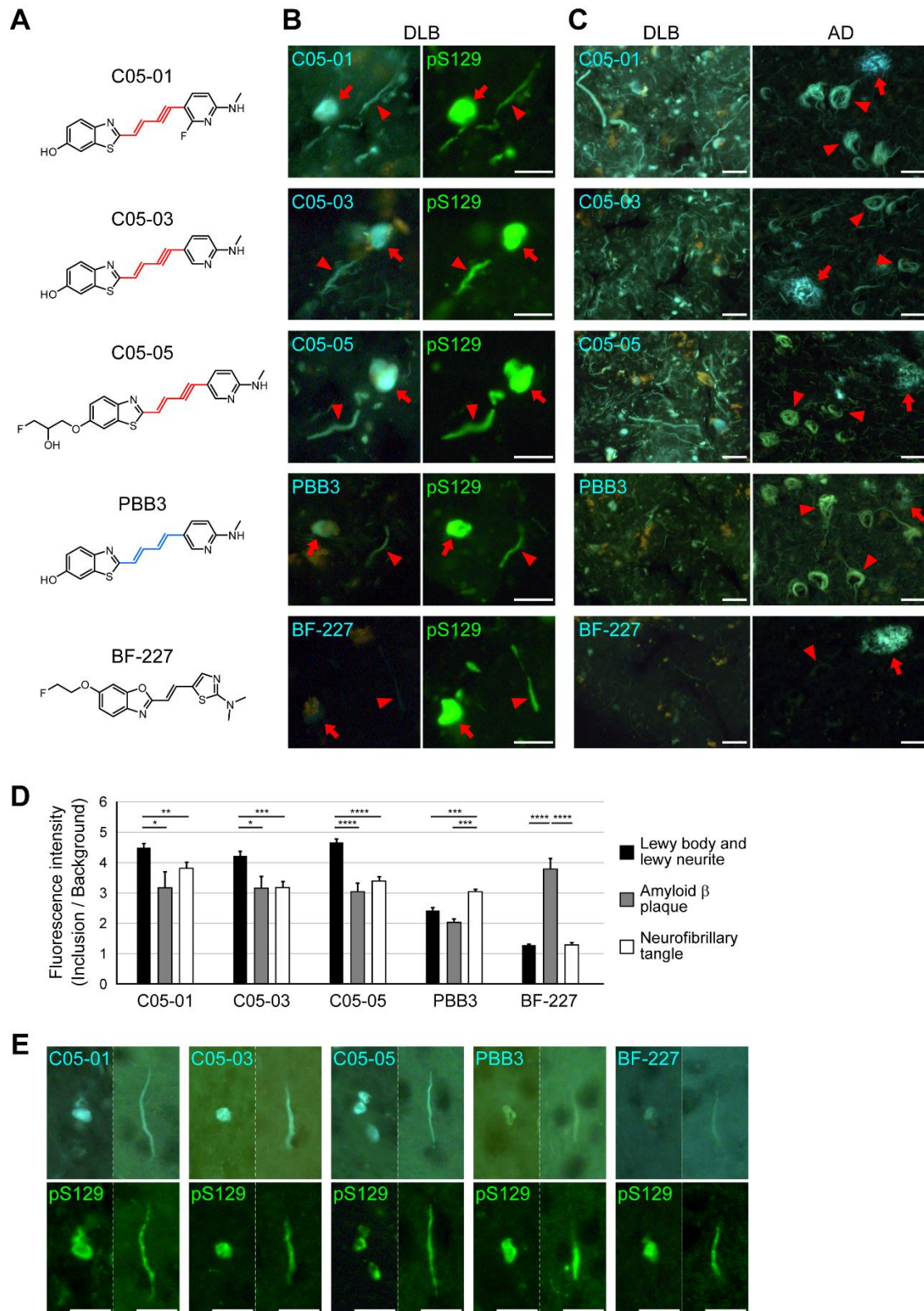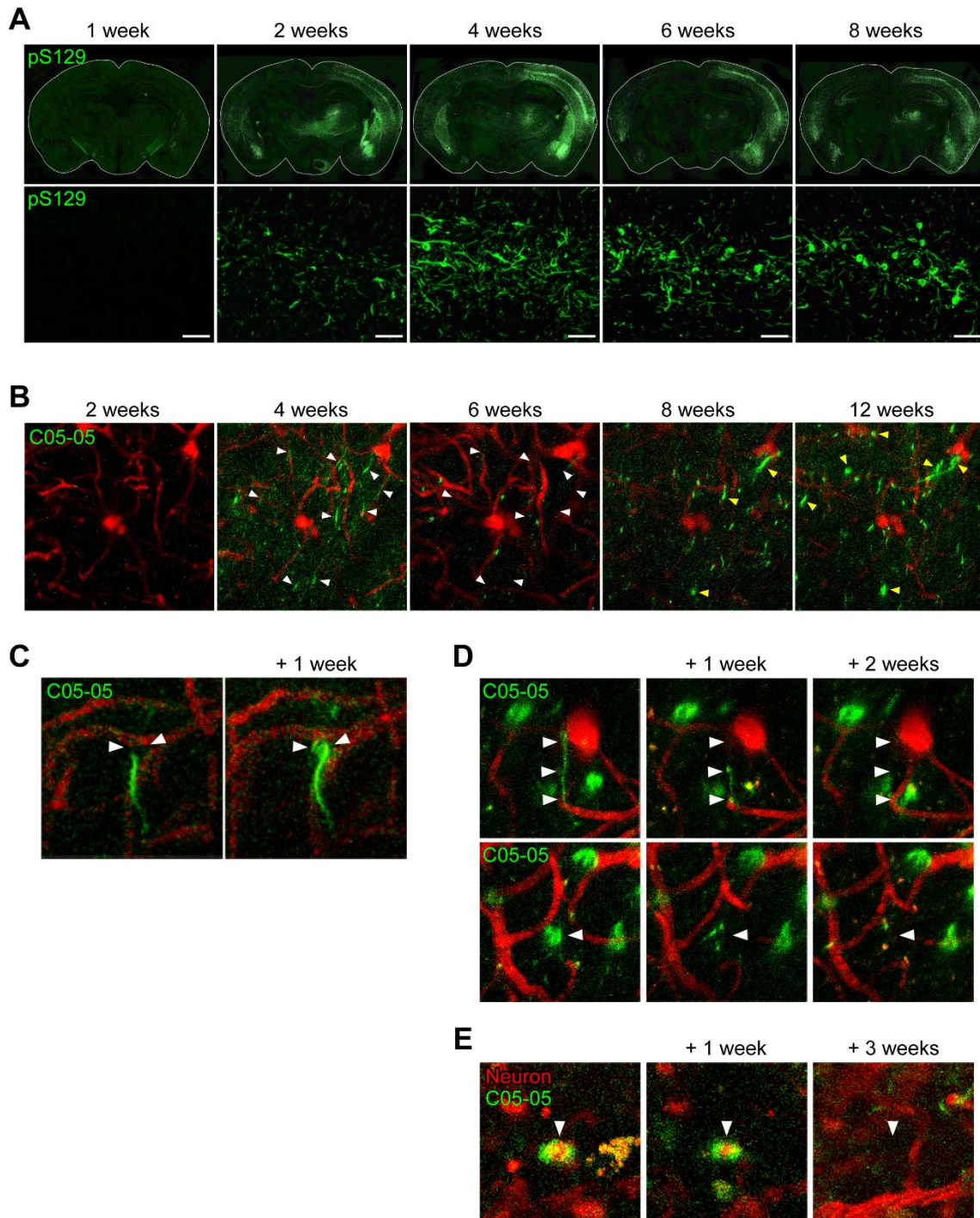
Figure 1. C05 series compounds bind to α-synuclein inclusions in DLB and mouse model of α-synucleinopathy *in vitro*.
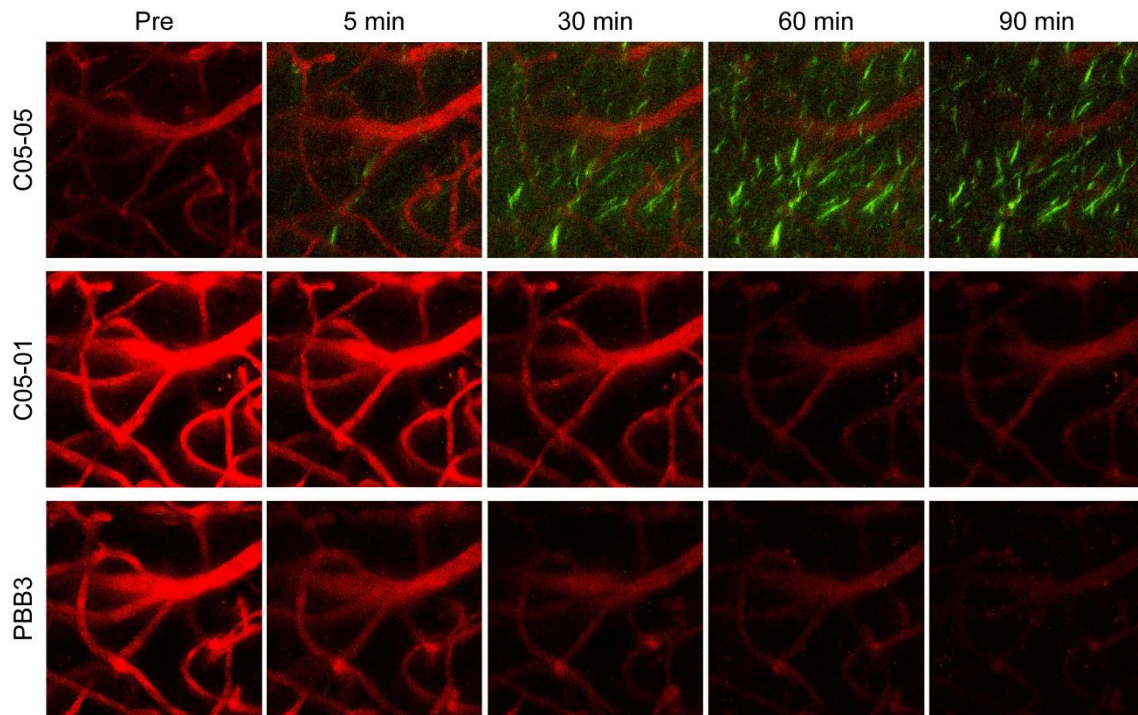
Figure 2. C05-05 enables *in vivo* optical visualization of individual α-synuclein inclusions in the brain of an α-Syn mouse model.
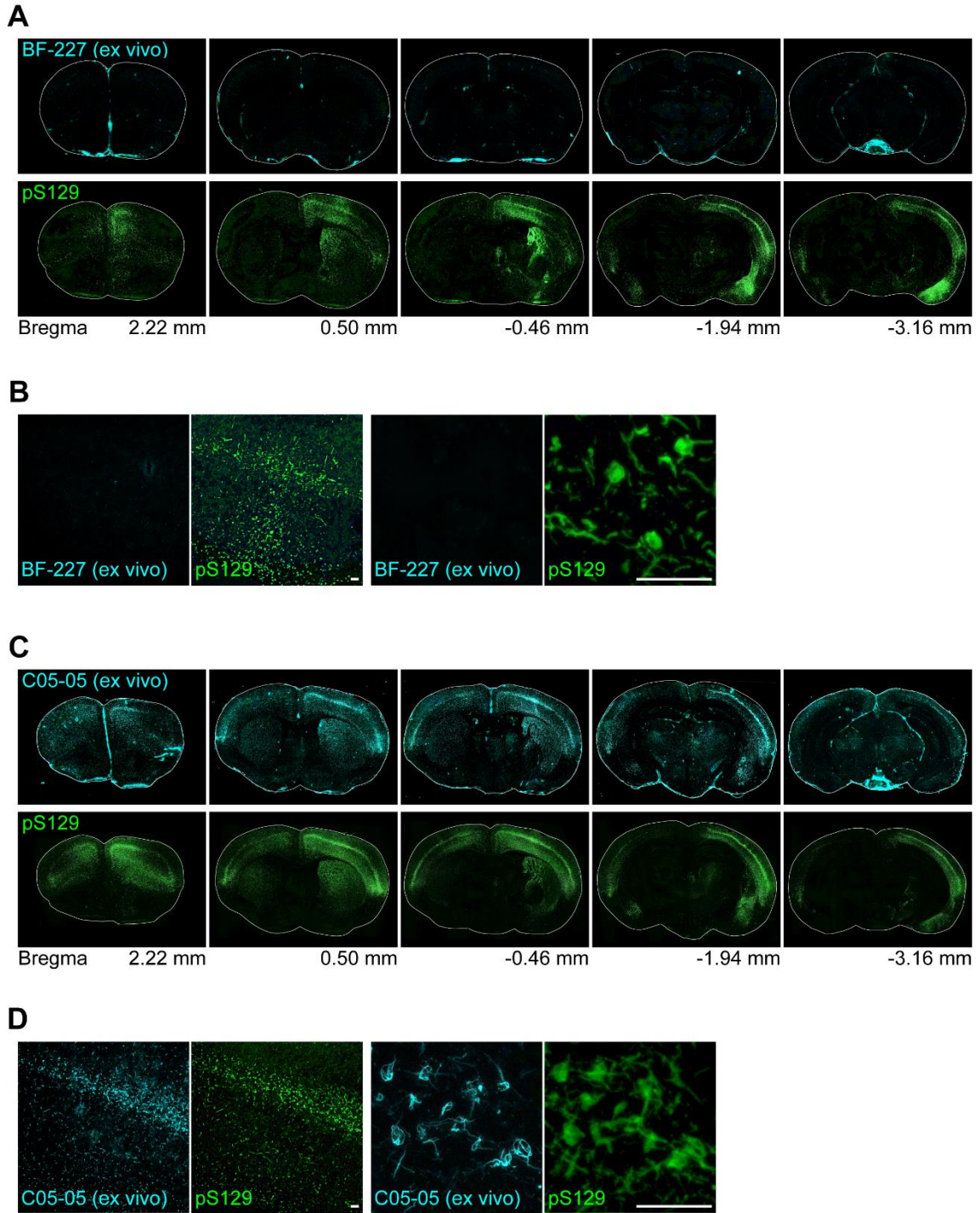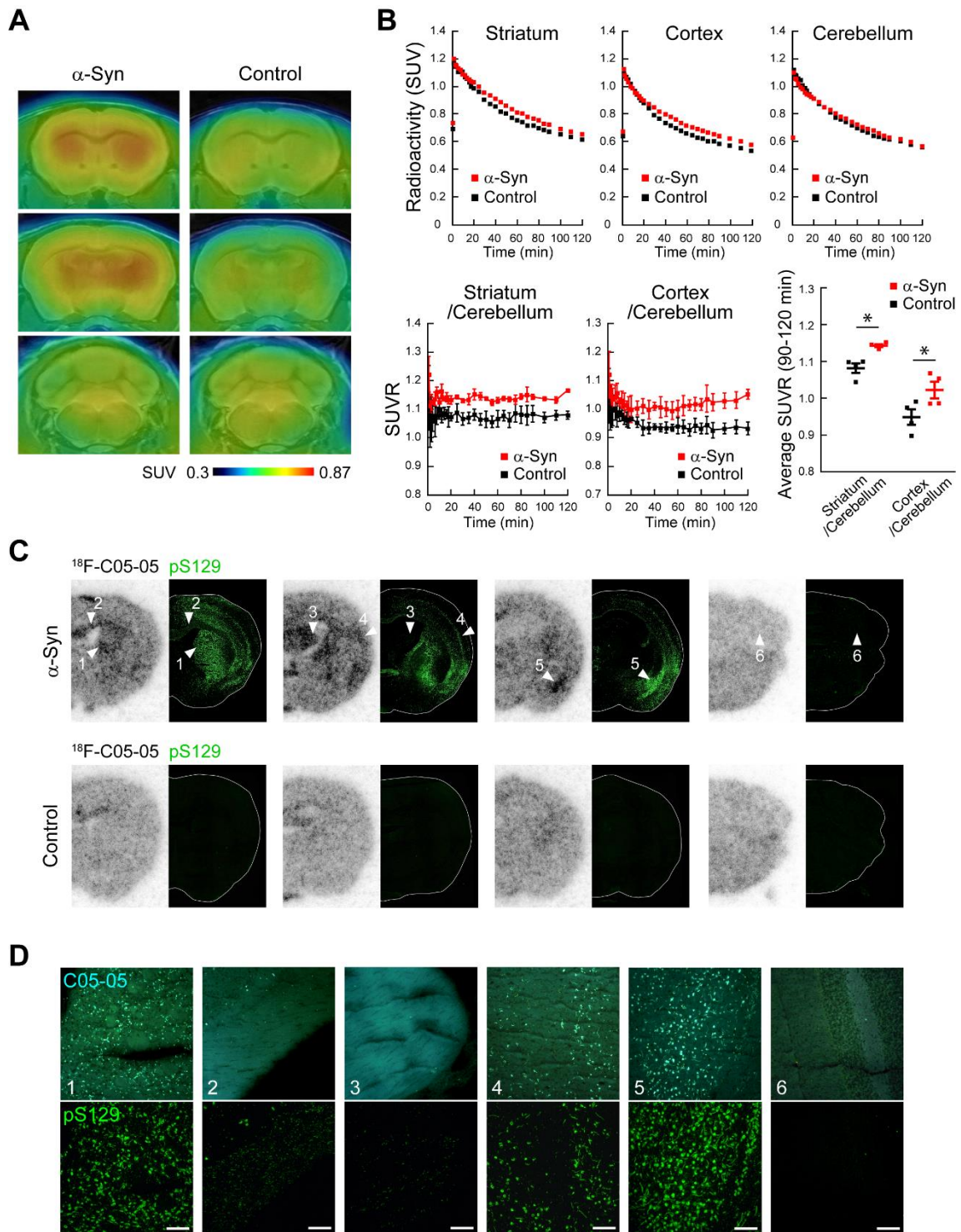
**Figure 3.** C05-05 enables *ex vivo* detection of α-synuclein inclusions in the brain of an α-synucleinopathy mouse model.

Figure 4. Pathological α-synuclein propagates to extensive brain areas with a transient oscillation of the aggregate amount in the brains of a living α-Syn mouse model.
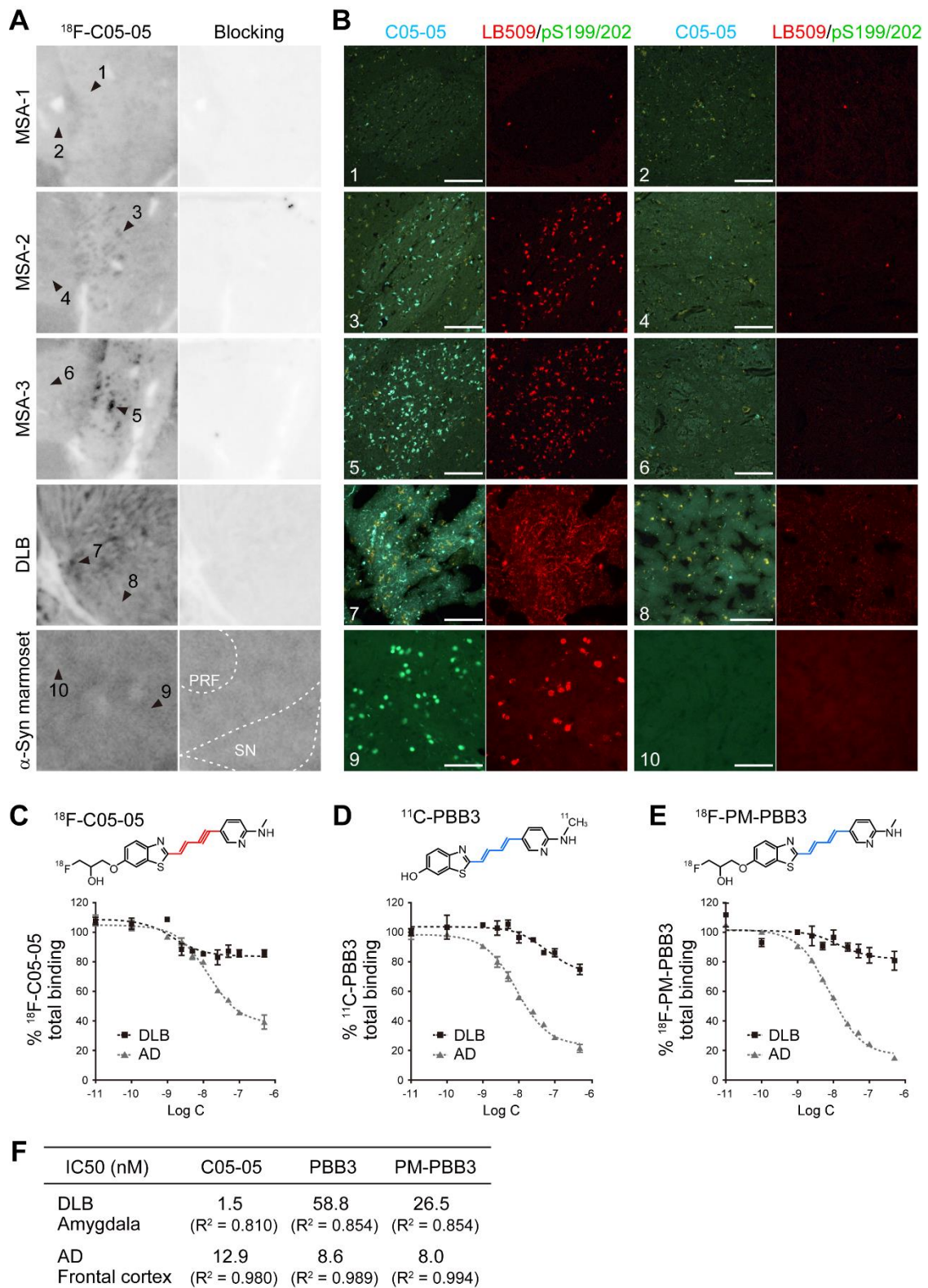
Figure 5. *In vivo* PET imaging with ^{18}F-C05-05 detects α-synuclein deposits in the brains of α-Syn mice.
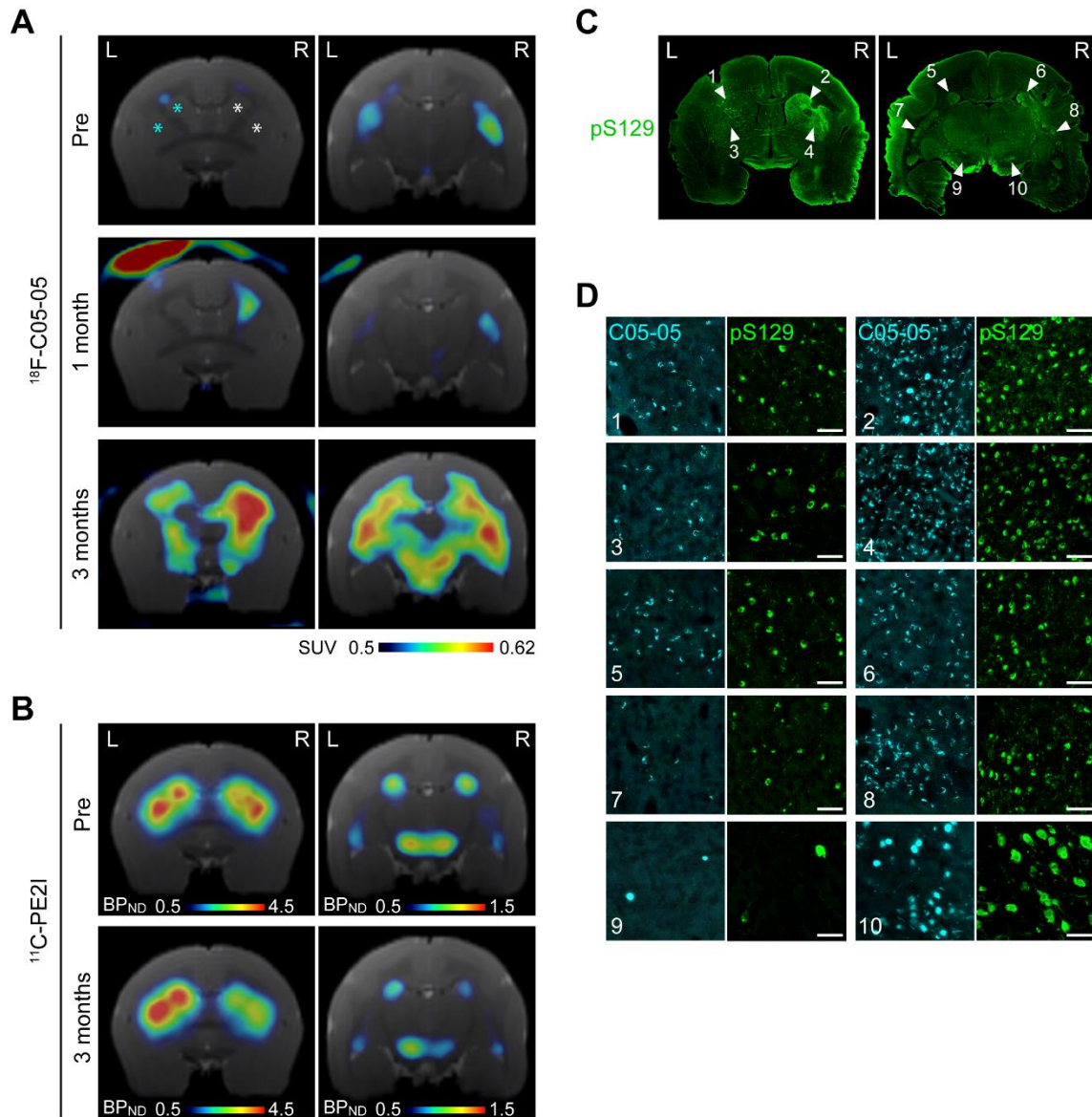
Figure 6. Longitudinal *in vivo* PET imaging with ^{18}F-C05-05 visualizes the propagation of pathological α-synuclein aggregates in the brain of an α-Syn marmoset.

Figure 7. ^{18}F-C05-05 displays high-affinity binding to α-synuclein pathologies in DLB and MSA brain tissues.

59